OECD MCCI Project
Small-Scale Water Ingression and Crust Strength Tests (SSWICS)
SSWICS-1 Final Data Report

Rev. 1 February 10, 2003

by:

S. Lomperski, M. T. Farmer , D. Kilsdonk, B. Aeschlimann

Reactor Analysis and Engineering Division
Argonne National Laboratory
9700 S. Cass Avenue
Argonne, IL 60439
USA

Table of Contents

Appendix A: List of Plots

1. Introduction

The Melt Attack and Coolability Experiments (MACE) program at Argonne National Laboratory addressed the issue of the ability of water to cool and thermally stabilize a molten core/concrete interaction (MCCI) when the reactants are flooded from above. These tests provided data regarding the nature of corium interactions with concrete, the heat transfer rates from the melt to the overlying water pool, and the role of noncondensable gases in the mixing processes that contribute to melt quenching. However, due to the integral nature of these tests, several questions regarding the crust freezing behavior could not be adequately resolved. These questions include:

1) To what extent does water ingression into the crust increase the melt quench rate above the conduction-limited rate and how is this affected by melt composition and system pressure?
2) What is the fracture strength of the corium crust when subjected to a thermal-mechanical load and how does it depend upon the melt composition?

A series of separate-effects experiments are being conducted to address these issues. The first employs an apparatus designed to measure the quench rate of a pool of corium (~ϕ30 cm; up to 20 cm deep). The main parameter to be varied in these quench tests is the melt composition since it is thought to have a critical influence on the crust cracking behavior which, in turn, alters quench rate. The issue of crust strength will be addressed with a second apparatus designed to mechanically load the crust produced by the quench tests. This apparatus will measure the fracture strength of the crust while under a thermal load created by a heating element beneath the crust. The two apparatuses used to measure the melt quench rate and crust strength are jointly referred to as SSWICS (Small-Scale Water Ingression and Crust Strength).

This report describes results of the first water ingression test, designated SSWICS-1. The test investigated the quench behavior of a 15 cm deep, fully oxidized PWR corium melt containing 8 wt% limestone/common sand concrete decomposition products. The melt was quenched at nominally atmospheric pressure. The report includes a description of the test apparatus, the instrumentation used, plots of the recorded data, and data reduction to obtain an estimate of the corrected heat flux from the corium to the overlying water pool. A section of the report is devoted to calculations of the conduction-limited heat flux that accounts for heat losses to the crucible holding the corium. The remainder of the report describes post test examinations of the crust, which includes permeability and mechanical strength measurements, and chemical analysis.

2. System Description

2.1 Test Apparatus

The SSWICS reaction vessel (RV) has been designed to hold up to 100 kg of melt at an initial temperature of 2500^{o}C. The RV lower plenum consists of a 67.3 cm long, 45.7 cm (18") outer diameter carbon steel pipe (figure 2.1). The pipe is insulated from the melt by a 6.4 cm thick

layer of cast MgO. The selected pipe and insulation dimensions result in a melt diameter of 30.5 cm and a surface area of 730 cm^2. The melt depth at the maximum charge of 100 kg is about 20 cm.

The RV lower flange is insulated with a 6.4 cm thick slab of cast MgO that spans the entire inner diameter of the pipe. The MgO slab and sidewalls form the crucible containing the corium. This particular geometry was chosen to facilitate removal of the slab for the crust strength measurement tests. Corium has a tendency to bond with the MgO insulation and this design allows one to pry the slab away from the MgO walls without damaging the crust.

The MgO slab lies beneath a 1.3 cm thick cast ZrO_2 plate. The ZrO_2 is added because of its exceptionally low thermal conductivity at high temperature (~1 W/m^oC, versus ~10 for MgO at 2000^{o}C). Despite its low thermal conductivity, the ZrO_2 is not used as the primary insulator to protect the flange because of its poor thermal shock resistance. To protect the cast ZrO_2 plate from the initial thermal shock following thermite ignition, a disk of low-density ZrO_2 board is set on top of the cast plate. This material is not structurally robust and serves as a sacrificial layer that absorbs the initial thermal shock of thermite ignition. Finally, a thin layer (0.25 mm) of tungsten is added in an effort to prevent the erosion of the ZrO_2 that is expected if the corium was allowed to come in direct contact with the low-density board.

The RV upper plenum consists of a second section of pipe lined with cast MgO. Three 10 cm pipes welded near the top of the vessel provide 1) a vent line for the initial surge of hot noncondensable gases generated by the thermite reaction, 2) a pressure relief line with a rupture disk (7.7 bar at 100^{o}C), and 3) an instrument flange for the absolute pressure transmitter that measures the reaction vessel pressure. Four 6 mm (¼") tubes serve as water inlets for melt quenching. A baffle is mounted below the upper flange and the water flow is directed towards the baffle to reduce the momentum of the fluid before it drops down onto the melt. The baffle is also intended to prevent water droplets from being carried up towards the condenser, which would adversely affect the heat flux measurement. A fourth 10 cm pipe welded to the top flange provides an outlet to carry steam from the quenching melt to four cooling coils. The water-cooled coils condense the steam, which is collected within a 200 cm high, 20 cm diameter condensate tank (CT). Figure 2.2 is a schematic that provides an overview of the entire SSWICS melt-quench facility.

2.2 Instrumentation

Instrumentation has been selected to provide all measurements necessary to determine the melt dryout heat flux. Tables 2.1 and 2.2 list the sensors and major valves, respectively.

The critical measurement for these tests is the steaming rate in the RV, which is found indirectly by measuring the rate of condensate collection in the CT. Two differential pressure sensors, PD1-CT and PD2-CT, are used to measure condensate inventory.

The remaining instrumentation provides supplementary information to further characterize the test conditions. The initial melt temperature is provided by two Type-C thermocouples located 20 mm above the bottom of the melt and 7.5 cm from the RV centerline (halfway to the MgO

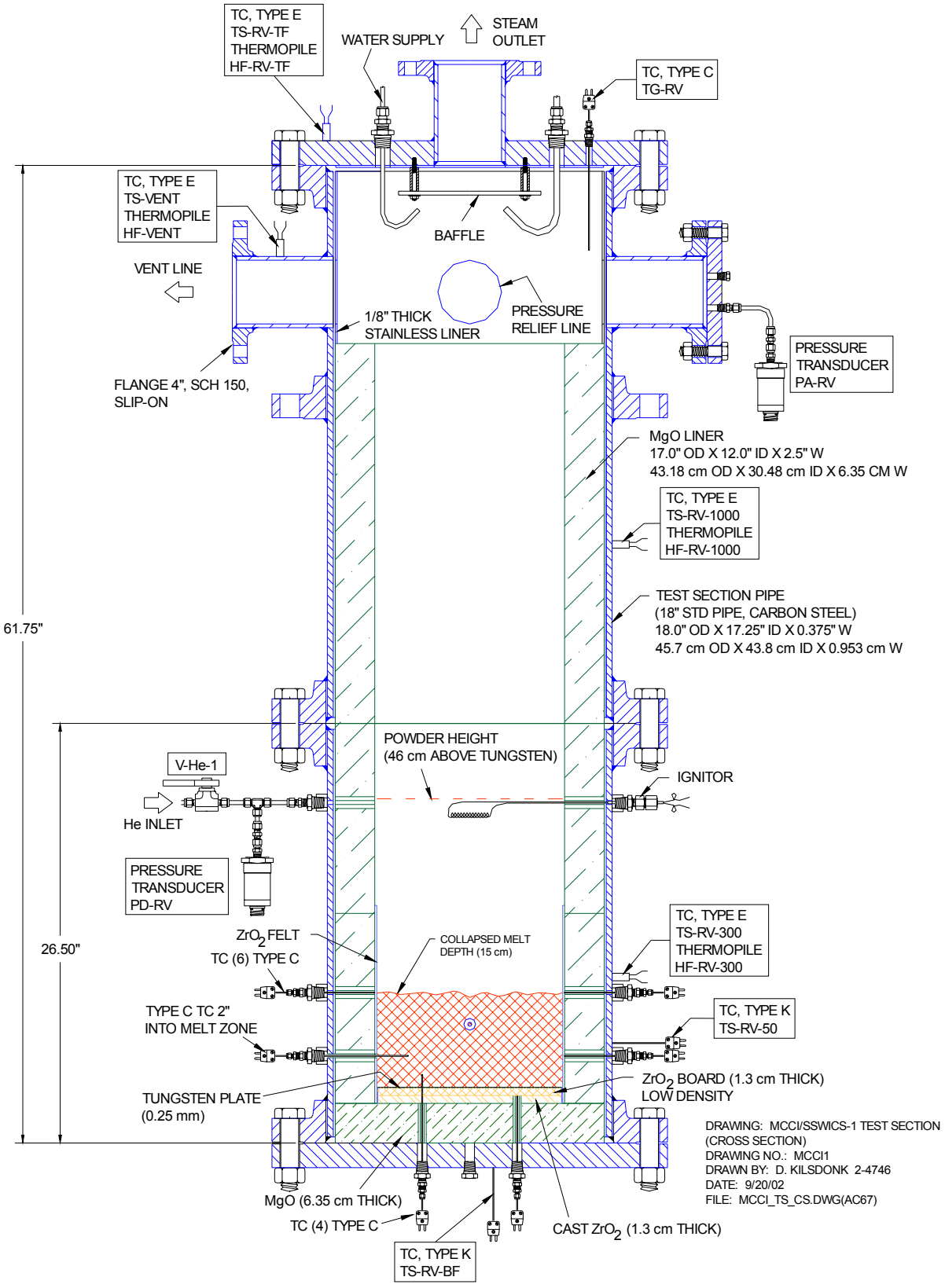

Figure 2.1 Side view of reaction vessel.

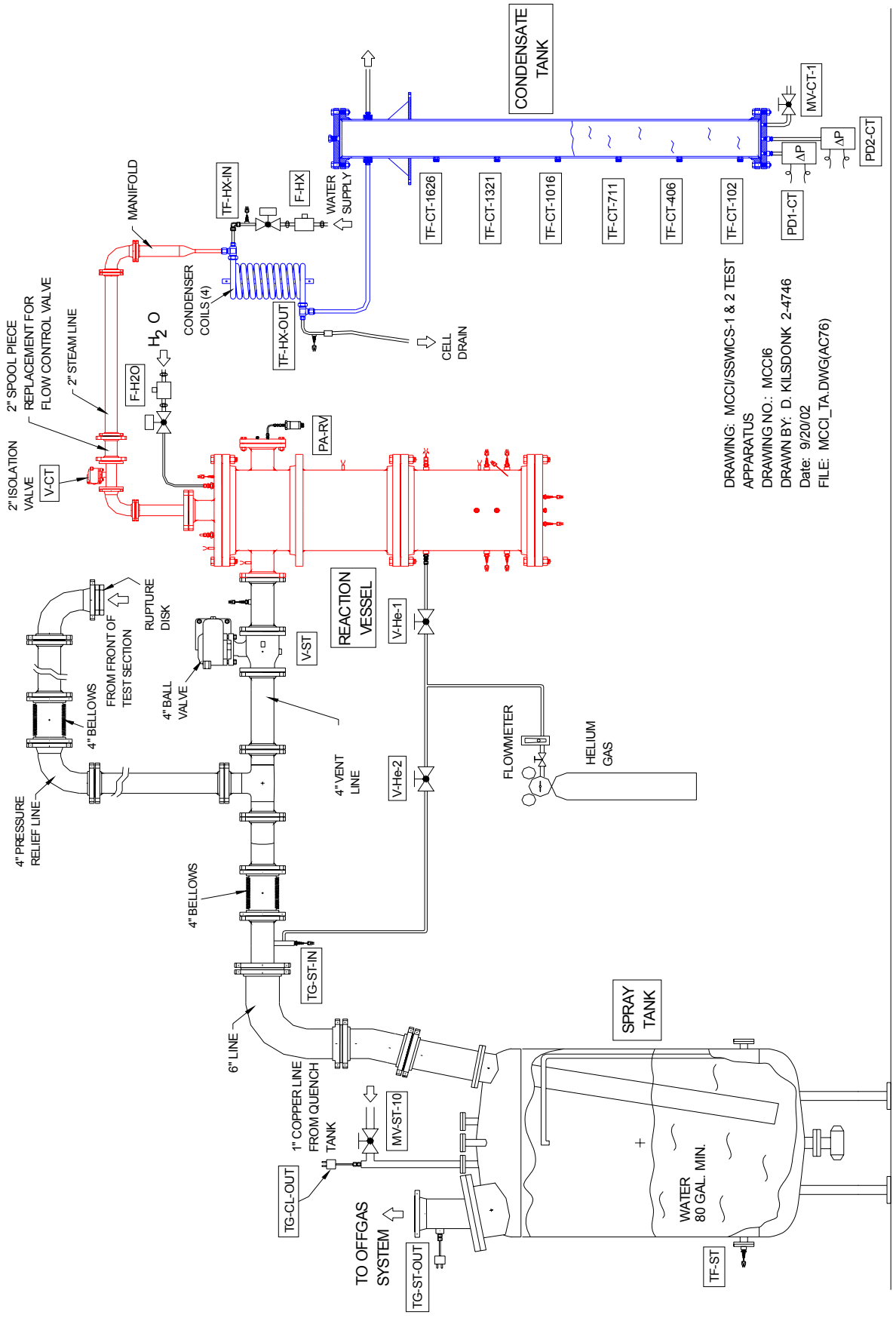

Figure 2.2 SSWICS melt quench facility.

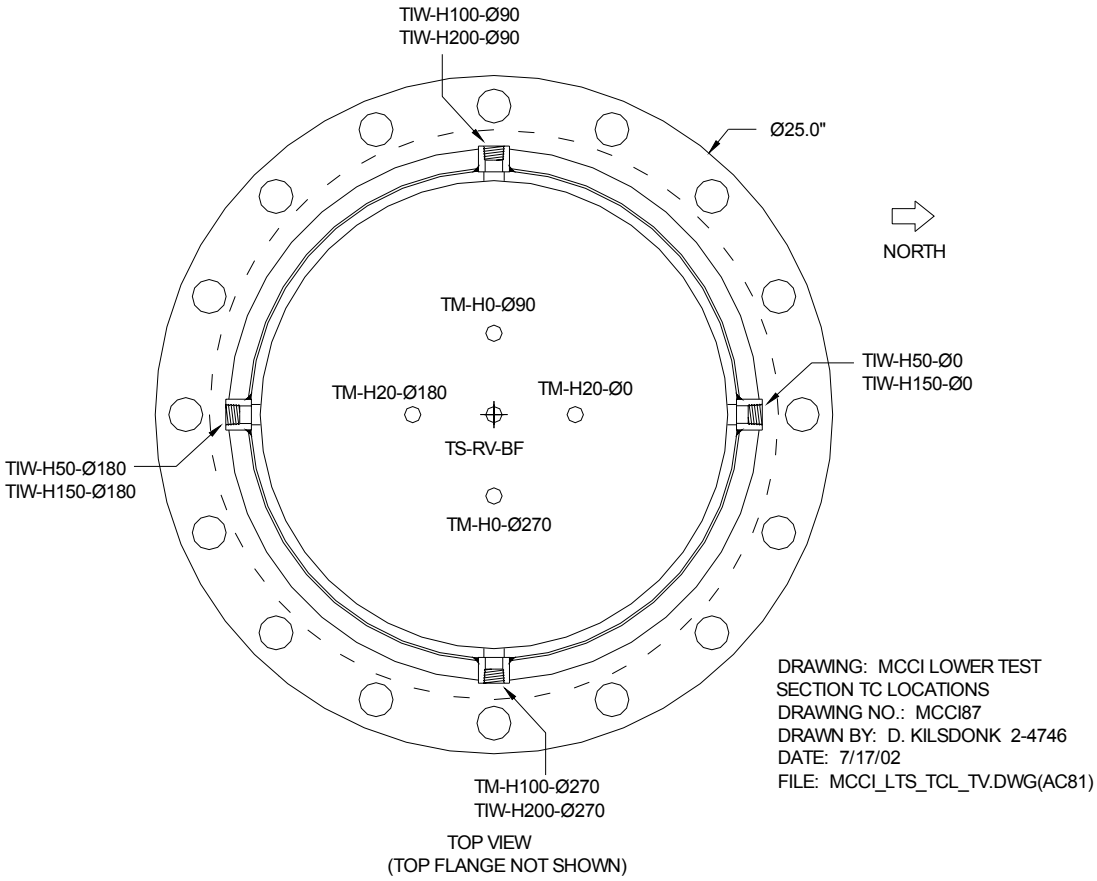

Figure 2.3 Reaction vessel thermocouple locations.

wall). A second pair of Type-C thermocouples below the ZrO_2 board and near the bottom of the melt is used to detect the arrival of the quench front. The melt is considered quenched when the temperature at the base of the melt reaches the saturation temperature, and this is the basis for terminating the test. Figure 2.3 illustrates the thermocouple locations within the RV. The nomenclature used to identify the thermocouples is as follows: TIW (temperature at the inner wall of the MgO insulator, TM (temperature within the corium melt), H# (height above the bottom of the melt, in mm, ϕ# (angle relative to direction north, in degrees). For example, TIW-50-ϕ180 is located at the inner wall of the MgO insulation, 50 mm above the bottom of the melt and south of the RV axis. Note that the four thermocouples penetrating the basemat are 76 mm from the RV centerline.

There are a total of eight locations near the base of the RV for radial instrument penetrations. One is reserved for a pyrometer to measure melt temperature at a level of 100 mm above the bottom of the melt. The tungsten thermowell necessary for this instrument was not yet available and so a C-Type thermocouple has been used in place of the pyrometer. The thermocouple was positioned with the tip 50 mm from the MgO wall (i.e., 50 mm into the melt).

Five of the remaining seven penetrations were used for thermocouples positioned at the outer edge of the melt to determine whether water seeps between the MgO wall and the crust as it forms above the melt. Though such seepage is deemed unlikely, this must be verified because

#	Channel	Name	Type	Description	Serial #	Output	Range	Accuracy
0	HPS-0	T-CJ-HPS	AD592 IC	Cold junction compensation sensor.	-	1μA/K	0-70°C	A 0.5°C
1	HPS-1	TM-H0-ϕ90	TC type C	Melt temp. at bottom of melt.	-	0-37 mV	0-2320°C	A 4.5°C or 1%
2	HPS-2	TM-H0-ϕ270	TC type C	Melt temp. at bottom of melt.	-	0-37 mV	0-2320°C	A 4.5°C or 1%
3	HPS-3	TM-H20-ϕ0	TC type C	Melt temp. 20 mm above bottom of melt.	-	0-37 mV	0-2320°C	A 4.5°C or 1%
4	HPS-4	TM-H20-ϕ180	TC type C	Melt temp. 20 mm above bottom of melt.	-	0-37 mV	0-2320°C	A 4.5°C or 1%
5	HPS-5	TIW-H50-ϕ0	TC type C	Melt temp. at inner sidewall 50 mm above bottom of melt.	-	0-37 mV	0-2320°C	A 4.5°C or 1%
6	HPS-6	TIW-H50-ϕ180	TC type C	Melt temp. at inner sidewall 50 mm above bottom of melt.	-	0-37 mV	0-2320°C	A 4.5°C or 1%
7	HPS-7	TIW-H100-ϕ90	TC type C	Melt temp. at inner sidewall 100 mm above bottom of melt.	-	0-37 mV	0-2320°C	A 4.5°C or 1%
8	HPS-8	TIW-H150-ϕ0	TC type C	Melt temp. at inner sidewall 150 mm above bottom of melt.	-	0-37 mV	0-2320°C	A 4.5°C or 1%
9	HPS-9	TIW-H150-ϕ180	TC type C	Melt temp. at inner sidewall 150 mm above bottom of melt.	-	0-37 mV	0-2320°C	A 4.5°C or 1%
10	HPS-10	TM-H100-ϕ270	TC type C	Melt temp. 50 mm from sidewall, 100 mm above bottom of melt.	-	0-37 mV	0-2320°C	A 4.5°C or 1%
11	HPS-11	RESERVE	-	-	-	-	-	-
12	HPS-12	TG-RV	TC type C	Gas temp. in reaction vessel upper plenum.	-	0-37 mV	0-2320°C	A 4.5°C or 1%
13	HPS-13	TS-RV-300	TC type E	Outer wall temp. of RV 300 mm above bottom of melt.	-	0-70 mV	0-900°C	A 1.7°C or 0.5%
14	HPS-14	TS-RV-1000	TC type E	Outer wall temp. of RV 1000 mm above bottom of melt.	-	0-70 mV	0-900°C	A 1.7°C or 0.5%
15	HPS-15	TS-RV-tf	TC type E	Temperature of RV top flange	-	0-70 mV	0-900°C	A 1.7°C or 0.5%
16	HPS-16	TS-vent	TC type E	Outer wall temp. of vent line.	-	0-70 mV	0-900°C	A 1.7°C or 0.5%
17	HPS-17	TS-RV-bf	TC type K	Temperature of RV bottom flange.	-	0-50 mV	0-1250°C	A 2.2°C or 0.75%
18	HPS-32	TS-RV-50	TC type K	Outer wall temp. of RV 50 mm above bottom of melt.	-	0-50 mV	0-1250°C	A 2.2°C or 0.75%
19	HPS-18	TF-CT-102	TC type K	Fluid temp. in condensate tank at a water level of 102 mm.	-	0-50 mV	0-1250°C	A 2.2°C or 0.75%
20	HPS-19	TF-CT-406	TC type K	Fluid temp. in condensate tank at a water level of 406 mm.	-	0-50 mV	0-1250°C	A 2.2°C or 0.75%
21	HPS-20	TF-CT-711	TC type K	Fluid temp. in condensate tank at a water level of 711 mm.	-	0-50 mV	0-1250°C	A 2.2°C or 0.75%
22	HPS-21	TF-CT-1016	TC type K	Fluid temp. in condensate tank at a water level of 1016 mm.	-	0-50 mV	0-1250°C	A 2.2°C or 0.75%
23	HPS-22	TF-CT-1321	TC type K	Fluid temp. in condensate tank at a water level of 1321 mm.	-	0-50 mV	0-1250°C	A 2.2°C or 0.75%
24	HPS-23	TF-CT-1626	TC type K	Fluid temp. in condensate tank at a water level of 1626 mm.	-	0-50 mV	0-1250°C	A 2.2°C or 0.75%
25	HPS-24	TF-HX-in	TC type K	Fluid temp. at HX coolant inlet.	-	0-50 mV	0-1250°C	A 2.2°C or 0.75%
26	HPS-25	TF-HX-out	TC type K	Fluid temp. at HX coolant outlet.	-	0-50 mV	0-1250°C	A 2.2°C or 0.75%
27	HPQ-51	TF-ST	TC type K	Fluid temp. in spray tank.	-	0-50 mV	0-1250°C	A 2.2°C or 0.75%
28	HPQ-53	TG-ST-in	TC type K	Gas temp. in the spray tank line inlet.	-	0-50 mV	0-1250°C	A 2.2°C or 0.75%
29	HPQ-54	TG-ST-out	TC type K	Gas temp. in the spray tank line outlet.	-	0-50 mV	0-1250°C	A 2.2°C or 0.75%
30	HPS-26	HF-RV-300	Thermopile	Heat Flux through RV wall 300 mm above bottom flange.	0629	0-5.72 mV	0-5 kW/m^2	A 3%
31	HPS-27	HF-RV-1000	Thermopile	Heat Flux through RV wall 1000 mm above bottom of flange.	0630	0-5.19 mV	0-5 kW/m^2	A 3%
32	HPS-28	HF-RV-tf	Thermopile	Heat Flux through RV top flange.	0631	0-5.56 mV	0-5 kW/m^2	A 3%
33	HPS-29	HF-vent	Thermopile	Heat Flux through connecting line to V-ST.	0632	0-5.50 mV	0-5 kW/m^2	A 3%
34	HPS-30	RESERVE	-	-	-	-	-	-
35	HPS-31	I-ign	DC supply	Current supply for thermite ignitor.	-	0-100 mV	0-25 Amps	-
36	HPS-33	PA-RV	1810AZ	Absolute pressure in reaction vessel.	2	0-12 V	0-4 bar	A 0.03 bar

Table 2.1 Instrumentation list (part 1 of 2).

#	Channel	Name	Type	Description	Serial #	Output	Range	Accuracy
37	HPS-34	PD-RV	1801DZ	Gauge pressure at	D-2	0-13 V	0-0.35 bar	A 0.004 bar
38	HPS-35	PD1-CT	1801DZ	Level of condensate in quench tank measured by DP transmitter.	D-9	0-13 V	0-0.35 bar	A 0.004 bar
39	HPS-36	PD2-CT	1801DZ	Level of condensate in quench tank measured by DP transmitter.	D-4	0-13 V	0-0.35 bar	A 0.004 bar
40	HPS-37		-	Voltage of the power supply for the pressure transmitters.	-	0-15 V	-	-
41	HPQ-50	T-CJ-HPQ	AD592 IC	Cold junction compensation sensor.	-	1μA/K	0-70°C	A 0.5°C
42	HPQ-52	TG-CL-out	TC type K	Gas temperature in condensate tank outlet line to spray tank.	-	0-50 mV	0-1250°C	A 2.2°C or 0.75%
43	HPQ-55	F-quench	Paddlewheel	Flow rate of cold water to heat exchangers.	3143	0-5 V	0-50 gpm	A 0.5 gpm
44	HPQ-56	F-HX	Paddlewheel	Flow rate of water into reaction vessel (for quenching melt).	3180	0-5 V	0-18 gpm	A 0.18 gpm

Table 2.2 Instrumentation list (part 2 of 2).

Channel #		Valve Name	Type	Description	Actuator
1		V-CT	Ball valve	Valve on steam line between reaction vessel and quench tank.	Pneumatic
2		V-quench	Ball valve	Valve on quench water supply line into reaction vessel.	Solenoid
3		V-H2O-i	Ball valve	Isolation valve on quench water supply line into reaction vessel.	Solenoid
4		V-H2O-b	Ball valve	Bypass valve on quench water supply line into reaction vessel.	Solenoid
5		V-ST	Ball valve	Valve on vent line between reaction vessel and spray tank.	Pneumatic
-		V-HX	Ball valve	Valve on cooling-water line to heat exchangers.	Solenoid

Table 2.3 Remotely operated valves.

Parameter	SSWICS-1
Test section internal diameter (cm)	30.5
Melt composition (wt % UO_2/ZrO_2/Cr/Concrete)	61/25/6/8
Concrete type	LCS
Melt mass (kg)	75
Initial Melt Temperature (°C)	~2300
Basemat type	Inert
System pressure (bar)	1
Water injection flowrate (lpm)	4
Water injected (liters)	33

Table 3.1 Test specifications forSSWICS-1.

Constituent	Mass (kg)
U_3O_8	47.26
CrO_3	9.24
CaO	2.34
Zr	13.82
Mg	0.52
Si	0.77
SiO_2	0.88
Al	0.17
Total	75.0

Constituent	Wt %	
	Reactant	Product
U_3O_8	63.01	-
UO_2	-	60.62
Zr	18.42	-
ZrO_2	-	24.90
Si	1.03	-
SiO_2	1.18	3.39
Mg	0.69	-
MgO	-	1.14
Al	0.22	-
Al_2O_3	-	0.41
CaO	3.13	3.13
CrO_3	12.32	-
Cr	-	6.41

Tables 3.2 Corium powder charge and reaction product mass fractions.

the dryout heat flux measurement would be compromised by a melt that was partially cooled by water circumventing the crust. The remaining two instrument penetrations, located 200 mm above the bottom of the melt, were not used because they are about 50 mm above the expected top of the melt and thus would not yield any useful information.

Four heat flux meters were used to obtain direct measurements of local heat losses. Two sensors were attached to the side of the RV, a third to the top flange, and the fourth was mounted to the 4" vent line between the RV and valve V-ST. The entire RV was insulated from the melt level upwards. Though the insulation around the upper plenum should ensure that heat losses are small compared to the heat transfer rate through the cooling coils, the heat flux sensors provide an added reduction in uncertainty in the energy balance used to calculate heat flux from the corium melt. The lower 25 cm of the RV was left uninsulated so that any excessive wall heating or corium breach can be readily observed.

3. Test Parameters and Course of Test

The specifications for this test are listed in table 3.1. The measured masses of the constituents of the corium powder charge are listed in table 3.2. The 75 kg charge was selected to produce an approximate melt depth of 15 cm. Measured parameters are plotted in appendix A.

Shortly before thermite ignition, the valves were positioned so that ignition gases would be vented directly into the spray tank (i.e., valve V-ST open and valve V-CT closed). The helium gas flow of 10 slpm, which had been used to maintain an inert atmosphere within the reaction vessel during the 24 hours since the charge was loaded, was switched to the vent line (see fig. 2.2). Water flow to the heat exchanger was set at 42 l/min.

The igniter coils were energized to initiate thermite ignition and, within five seconds, an increase in the upper plenum gas temperature TG-RV was detected. After another ten seconds, thermocouples in the melt indicated a rise in temperature. The signal from the igniter has not been included in any graph in this report, but all data has been plotted with the initial signal to the igniter as the x-axis origin.

Most thermocouples located in or near the melt rose rapidly, ~500-750^{o}C/s and a molten pool was achieved in less than 30s after energizing the igniter. Figure A.1 shows the first eight minutes of the transient (all plots are attached as an appendix). Two of the three thermocouples positioned directly within the melt indicated a peak local temperature near 2300^{o}C. The thermocouple extending 50 mm into the melt (TM-H100-ϕ270) failed in less than one minute (most likely within seconds after reaching the peak temperature). The other two thermocouples survived for several minutes and appear to indicate that the target initial minimum temperature of 2200^{o}C was successfully surpassed.

The next phase of the experiment was the initial quench of the melt. Seventy-five seconds after ignition, valve V-CT was opened so that steam would be able to travel to the heat exchangers. Valve V-ST was closed at 89 s to isolate the vent line and spray tank from the system. Water injection was initiated at 140 s at a flow rate of 3 l/min, lasting for 11 minutes (ending at 805 s) and resulting in an integrated flow of approximately 33 liters.

The plots of RV structure temperatures show the upper sidewalls rising to the saturation temperature within 500 s, before the injection phase has ended, indicating that the water pool was boiling during the majority of the injection phase.

No further action was taken until 6254 s, when V-quench was opened to add makeup water. The valve was open until 6328 s, injecting a total volume of about 3.8 liters. The valve was again open from 7150 s to 7202 s to inject another 2.7 liters. The second and third water injections were initiated out of concern that the pool above the corium might be drying out. However, figure A.7 confirms that the corium was always fully covered with liquid.

4. Sensor Malfunctions and Abnormalities

Post test examination of the test apparatus and a preliminary review of the data indicate the following:

1) The differential pressure measurement PD-RV probably failed due to melting and likely closure of the steel tube connecting the sensor's input pressure port and the RV lower plenum. This tube passes through the MgO liner and stops just short of the inner wall. It appears that despite the distance from the melt and protection of the MgO, the tube could not withstand the ignition phase and the end was melted partially or completely shut.
2) Sensor TM-H100-ϕ270 failed less than one minute into the test, TM-H20-ϕ0 failed at 1855 s, and TM-H20-ϕ180 failed at about 520 s.
3) The vent line between the RV and valve V-ST was mistakenly left uninsulated, as illustrated by heat flux meter HF-vent. This results in a small increase in vessel heat loss.
4) A sudden, small drop in RV pressure and a modest power surge to the heat exchanger took place near 2780 s and lasted about three minutes (figs. A.5 and A.8). This small transient preceded a monotonic (until near end of test) decline in the system heat load. Note that there were no operator actions during the ~30 minutes between the end of the initial water injection phase and the surge to the HX.
5) Sensor PD1-CT exhibited a relatively sudden jump of about 6 cm of H_2O shortly after the transient described above. Such a large surge of condensate is deemed unlikely and it is noted that the increase was not duplicated by sensor PD2-CT. It is believed that the tubing between the CT and the transducer had not been properly purged of air and the sudden pressure increase was due to air escaping the tube and being replaced with water.

5. Data Reduction

The main objective of the quench test is to measure the time-varying heat flux through the corium surface to the overlying layer of water (denoted q''). This is compared to the calculated conduction-limited heat flux, q_c'', to establish whether heat transfer is enhanced by some mechanism such as crack propagation within the crust. The corium heat flux is not measured directly, but is derived from an energy balance using the measured steam flow rate out of the

RV. The energy balance is adjusted with corrections such as sensible heat addition to the coolant and the heating of RV structures, both of which reduce the measured steam flow rate.

The conduction-limited heat flux is calculated using a 3-D model of the RV lower plenum. A 1-D model would be sufficient in the case of a very large-diameter corium pool or a perfectly insulating crucible. In our case, however, a multi-dimensional model is necessary to account for the substantial energy transfer from the corium to the MgO crucible, which lowers q_c" below that of the 1-D case. Proper characterization of heat transfer to the crucible is essential for obtaining the correct value of q_c", which in turn enables a meaningful comparison with q".

The remainder of section five is devoted to describing the methodology used to determine q". Section 5.1 notes the basic calculations used to obtain a first-order estimate of q" and sections 5.2 and 5.3 detail corrections to it. Section 6 is devoted to the analytical model used to determine q_c".

5.1 First order estimate of heat flux

A few basic aspects of the test are obtained with simple calculations. These include the RV coolant inventory and first order estimates of heat flux at the corium surface. The first parameter of interest is the coolant inventory in the RV as a function of time. The inventory is the difference between the total amount of liquid injected and the amount boiled off and collected in the CT:

$$M_{RV} = \sum_{t=0}^{t=t_{end}} \rho \dot{V} \Delta t \quad - \quad \frac{\pi}{4} D^2 \frac{\Delta P}{g} \tag{5.1}$$

where data from sensor F-quench is used for the volumetric flow rate $\dot{V}$ and the liquid density ρ is taken to be 998 kg/m^3. The condensate inventory is calculated with readings from sensor PD2-CT (ΔP) and the tank diameter D of 0.203 m. Figure A.7 shows both the integrated flow and CT inventory, labeled F-integrated and M-CT, respectively. The calculated net coolant inventory, denoted M-RV, confirms that the corium was always covered with water.

The corium heat flux was estimated using two methods, with each utilizing the steam flow rate from the RV. As a first order approximation, the steam flow rate out of the RV is equal to the evaporation rate near the corium surface. In this case, the heat of vaporization can be used to calculate the heat transfer rate from the corium. The first method considers the rate of condensate collection, which is a measure of the steam flow rate from the RV. The condensation rate is calculated from the time derivative of the differential pressure signal PD2-CT. The heat transfer rate from the corium is then:

$$Q_{CT} = \frac{1}{g} \frac{\pi}{4} D^2 \frac{\partial \Delta P}{\partial t} h_{fg} \tag{5.2}$$

where D is again the inner diameter of the CT and the heat of vaporization h_{fg} is 2257 kJ/kg^{o}C. The heat flux, shown in figure A.12, is obtained by scaling Q_{CT} with the cross-sectional area of the test section (0.071 m^2). The derivative was calculated with pairs of averaged ΔP readings (an average of 5 measurements at 0.5 Hz) centered around a Δt of 60 s. The averaging and length of Δt were necessary to reduce oscillations in the calculated heat flux.

The second method of calculating corium heat flux uses an energy balance on the secondary side of the heat exchanger. The measured parameters are the coolant flow rate on the secondary side of the cooling coils and the inlet and outlet fluid temperatures. The cooling power of the heat exchanger is then:

$$Q_{HX} = \dot{V}_{HX} \rho c_p \left(T_{out} - T_{in}\right) \tag{5.3}$$

where readings from sensors TF-HX-in and TF-HX-out were used for temperatures T_{in} and T_{out}, respectively. Data from flow meter F-HX was used for $\dot{V}_{HX}$, and c_p and ρ are taken to be 4.18 kJ/kg^{o}C and 998 kg/m^3, respectively. The heat flux calculated with the energy balance method is shown in figure A.12.

Two methods for determining the corium heat flux have been presented: a mass balance on the condensate tank (eqn. 5.2) and an energy balance on the condenser (5.3). As seen in figure A.12, these two methods yield similar results and so, for the sake of brevity, only one will be used for the remaining calculations in this report. The energy balance across the heat exchanger is chosen because the noise level of the signal is much lower.

5.2 Corrected heat flux

As noted earlier, to a first approximation, the condensation rate within the condenser equals the evaporation rate near the corium surface and so the heat of vaporization can be used to directly calculate the heat flux *q"*. For an accurate measure of *q"* this simple portrayal of the system is inadequate, especially early in the transient. During the water injection phase of the test, energy is absorbed by the coolant as it is heated to the saturation temperature. Also, early in the transient, steam condenses on relatively cold RV structures until they reach the saturation temperature. Both these effects reduce the amount of steam reaching the condenser and thus the apparent heat flux. Heat losses from the RV to the ambient also reduce steam flow to the condenser. A more accurate formulation of the heat flux must account for these various heat sinks:

$$q'' = \frac{1}{A}\left[Q_{HX} + Q_{sen} + Q_{str} + Q_{HL}\right] \tag{5.4}$$

where A is the corium surface area (0.071 m^2), Q_{HX} the measured cooling power of the heat exchanger, Q_{sen} the rate of sensible energy deposition into the coolant, Q_{str} the rate of energy absorption by the RV structures due to steam condensation, and Q_{HL} represents heat losses from the RV. The heat loss term was found to be small compared to the other terms and so it is neglected in the calculations.

The rate of sensible energy deposition into the coolant is difficult to determine precisely. Steam production and the addition of subcooled water occurred simultaneously during the first phase of the test. While it is clear that all the liquid was eventually heated from ambient to saturation temperature, it is uncertain how quickly the water was heated after entering the RV. In the early stage of water injection, liquid was immediately heated to the boiling point because the corium surface was far above the saturation temperature and the liquid inventory was low. During this period the rate of sensible heat addition can be obtained directly from the water injection rate $\dot{V}_q$:

$$Q_{sen} = \dot{V}_q \, \rho \, c_p (100 - T_{in}) \tag{5.5}$$

where $\dot{V}_q$ is obtained from flow meter F-quench and T_{in} is again TF-HX-in (the heat exchanger and quench supply draw water from the same source). The rate of sensible heat addition is plotted in figure 5.1 and is scaled by the corium surface area for comparison with the heat flux calculated using the heat exchanger energy balance.

The above relation is less appropriate for the latter part of the injection phase. As the corium surface cools and the depth of the overlying water layer increases, it becomes increasingly difficult to heat newly added water to saturation as quickly as it is injected. This is demonstrated by a sharp drop in the steaming rate late in the injection phase (figure A.8), indicating that the water pool temperature probably dropped briefly below the saturation temperature. Since there is no measurement of the pool temperature (placement of a thermocouple in the water pool is not feasible), it is not possible to accurately determine Q_{sen} during this late stage of water injection. Therefore the above equation, which provides a good estimate of Q_{sen} early in the injection phase and a less accurate estimate towards the end, will be used for the entire injection phase. The effect of this assumption is to slightly overestimate Q_{sen} towards the end of the injection phase since some of the sensible energy addition occurred after water injection ceased. In any event, this approach still ensures the proper total amount of energy addition to this heat sink.

The remaining term in eqn. 5.4 to be considered is Q_{str}, the rate of energy absorption by the RV structures. Early in the transient, Q_{str} is significant due to the combination of rapid temperature change and large structure heat capacity. Though the structures were kept to a minimum to reduce this effect, the vessel itself must be robust enough to withstand the combination of elevated temperature and pressure (for later tests). The thick-walled MgO liners also contribute to system heat capacity, but they serve the important function of protecting the vessel from the corium.

A precise calculation of Q_{str} requires knowledge of the time-dependent temperature distributions within the RV components, which can only be obtained with extensive instrumentation. A limited number of structure temperatures were measured during the test since it was thought that the early portion of the transient, when structure temperatures are changing, would be a small fraction of the total test duration. Once the system had heated to the saturation temperature, corrections associated with energy deposition into the structures would be negligible. However, the quenching process proceeded more rapidly than expected and so the period when heat sinks are significant is a larger fraction of the total test duration than anticipated. Thus it is worthwhile to attempt a correction for the early stage of the transient despite the limited instrumentation.

The rate of energy absorption by the structures can be written as:

$$Q_{str} = \sum_{i}^{N} M^i \, c_p^i \, \frac{\partial T^i}{\partial t} \tag{5.6}$$

where M represents mass, c_p specific heat, and T average temperature of a particular component. The summation is carried out over N components, which would include steel flanges, MgO liners, etc. The task of accounting for heat sinks is reduced by considering only the largest

system components. These are listed in table 5.1 to provide an indication of the relative importance of the various components as heat sinks.

A representative temperature must now be assigned to each of the system components. The only measured structure temperatures are those of the RV wall and flange (plotted in figure A.4). These are assigned to the largest steel RV components as described in table 5.1. The rate of energy deposition into a particular component is calculated from equation 5.6 using Δt=30 s (long enough to reduce the short term fluctuations in ΔT and short enough to retain acceptable time resolution in the result). Figure 5.1 shows the energy deposition rates for the selected components. As with the sensible heat addition to the injected water, the calculated power has been scaled by the corium surface area. The plot shows large peaks for the upper and lower plenums, which are a result of the rapid temperature changes of the RV walls. The thermocouples attached to the comparatively thick flanges show more modest peaks.

Though the sensors and structures have been matched in a reasonable fashion, the peak heat fluxes for the upper and lower plenums far surpass that of the heat exchanger, which is unrealistic. The cause of this disparity is the matching of wall temperature thermocouples to large masses that are made up, in part, of flanges that are much thicker than the walls. The walls change temperature more quickly than the flanges and so the rapid temperature rises shown by TS-RV-300 and -1000 are not indicative of the upper and lower plenum as a whole.

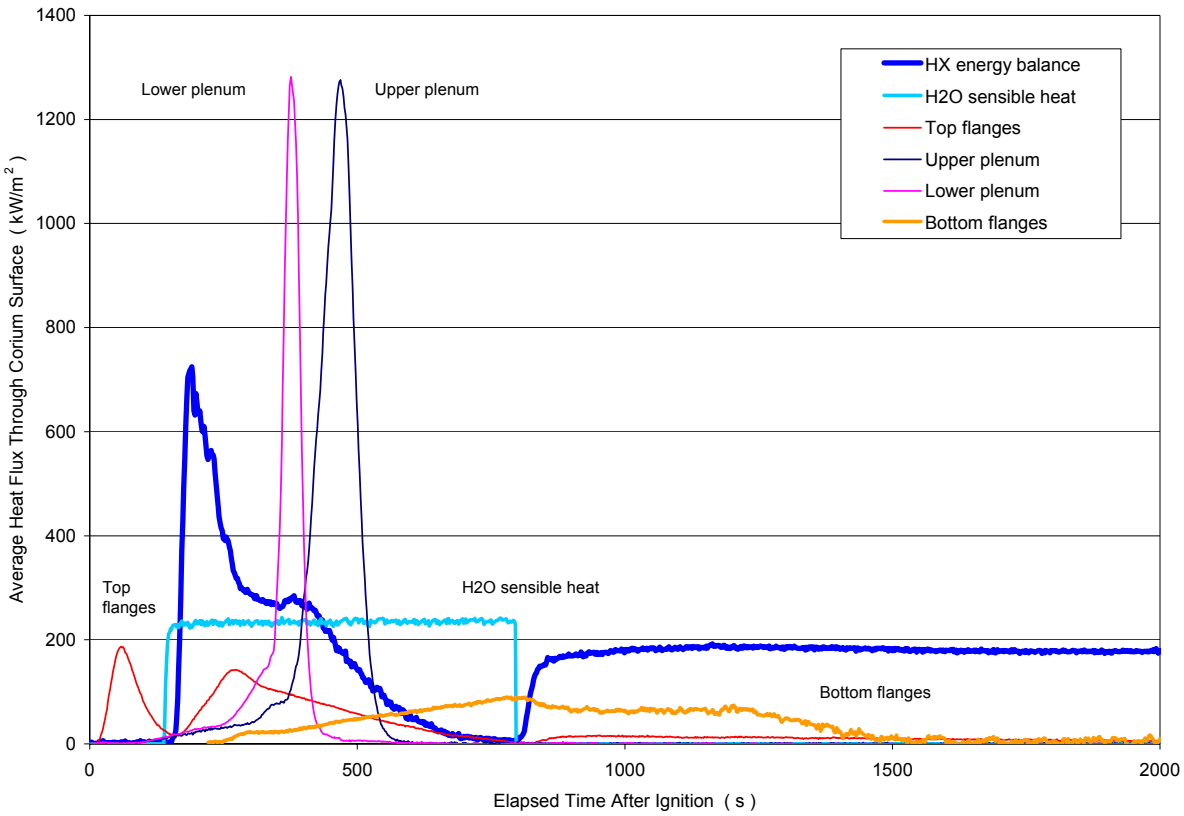

Figure 5.1 Scaled energy deposition rates into principal heat sinks.

The calculations suggest that there are an insufficient number of temperature sensors to accurately calculate the energy deposition rate into individual RV components during the early phase of the test. Moreover, there are no temperature measurements of the MgO liners, which comprise nearly half the structure heat capacity. It is concluded that there is not enough instrumentation to correct the energy balance on a component by component basis during the early phase of the test. It is proposed to use an alternative correction in which the heat capacities of all RV components are combined into a single component (table 5.1).

The energy deposition rate into the lumped structure is calculated using equation 5.6 and the parameters listed in table 5.1. The equation is simplified further to express an average power over a time Δt:

$$\overline{Q}_{str} = \sum_{i}^{N} M^{i} c_{p}^{i} \frac{(T_{sat} - T_{amb})}{\Delta t} \tag{5.7}$$

Selection of the period Δt is subjective because of the wide range of component time constants. The walls reached saturation temperature by t=500 s while the flanges (and presumably the MgO liners) were still heating after 1000 s. Note that water injection ended at 805 s and steam production resumed within the following minute. It is clear that the general trend of heat transfer to structures would be an initial peak in power, when all inner surfaces are at ambient temperature, followed by a monotonic decline such that some time after 1000 s the power is negligible. Since the effective time constant of the lumped structure is not known, Δt is set equal to the difference between the time water injection begins and the time steam flow returns to the heat exchanger (after injection is terminated). This is a reasonable compromise since *a)* a shorter Δt is unwarranted, as evidenced by the depressed load on the heat exchanger, which indicates energy is absorbed by heat sinks and b) there are no clear criteria for choosing a longer Δt and so the chosen period has the advantage of clarity. Furthermore, the sensible heat addition to the water will be added over the same interval to confine all corrections to the same period of the test.

One final note regarding the calculation of corrections: The water pool heat sink is assumed to absorb energy at constant power over the period of water injection, which is a satisfactory

Table 5.1 Principal heat sinks

Heat Sink	Material	Mass (kg)	c_p (J/kg K)	M c_p (kJ/K)	E* (MJ)	Associated Thermocouple
Top Flanges	Carbon Steel	150.	419.	63.	4.7	TS-RV-tf
Upper Plenum	Carbon Steel	245.	419.	103.	7.7	TS-RV-1000
Lower Plenum	Carbon Steel	140.	419.	59.	4.4	TS-RV-300
Bottom Flanges	Carbon Steel	150.	419.	63.	4.7	TS-RV-bf
Top MgO liner (24” long)	MgO	109.	1260.	137.	10.3	-
Middle MgO liner (12” long)	MgO	54.	1260.	68.	5.1	-
Lower MgO liner (upper 6”)	MgO	27.	1260.	34.	2.6	-
All structures	-	875.	-	527.	39.5	-
Injected Water	H_2O	33.	4180.	138.	10.8	TF-HX-in

* $E = M\, c_p\, \Delta T$; for structures and water $\Delta T = 75$ and $78^{o}C$, respectively.

assumption, as discussed previously. For the structures, however, the assumption is less satisfactory. As a slight refinement to the correction, it assumed that structure heating begins with a peak coinciding with the start of water injection, and then decreases linearly to zero after a time Δt. The peak power is twice Q_{avg}, as described in table 5.2.

Table 5.2 Heat sink corrections for figure 5.2

Heat Sink	E* (MJ)	t_1 (s)	t_2 (s)	Q_{avg} (kW)	q" (kW/m^2)
All structures	39.5	140	810	59.*	808.
Injected Water	10.8	140	810	16.	221.

* Correction in figure 5.2 uses $Q=2*Q_{avg} * [1 – (t –t_1)/ (t_2 – t_1)]$

5.3 Remarks regarding corrections

The suggested corrections to the heat flux are first-order, a fact that is highlighted by the discontinuity in the corrected flux soon after the end of water injection (figure 5.2). However, the approach has the advantage that it starts with a simple energy balance to establish the total amount of energy the heat sinks will absorb. This calculation should be fairly accurate. The simplification of constant power input to the water and structures is reasonable for the former but not for the latter. However, it allowed a correction without complex heat transfer calculations requiring in-vessel heat transfer coefficients that are not well-known. The correction is limited to the water injection period, which is considered to be the period of greatest heat transfer to the

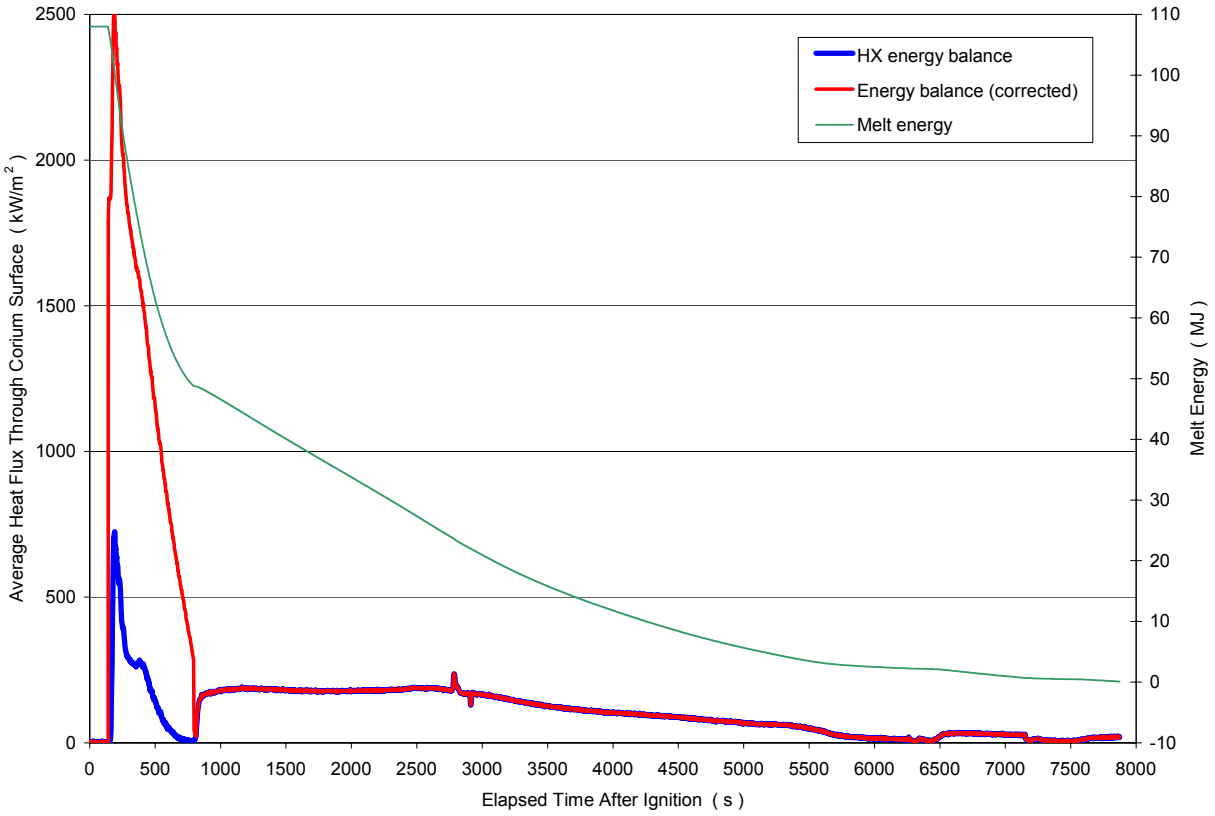

Figure 5.2 Scaled energy output from corium and total melt energy.

structures. With this simple approach, one can look at the data with a clear sense of what has been corrected and the magnitude of the correction.

But the considerable size of the correction encourages the development of a more realistic alternative. Figure 5.2 indicates that nearly 50% of the melt energy is absorbed by the heat sinks during the injection phase, which seems unreasonably high. In addition to the implausibly brief Δt for heat transfer to the structures, this is caused by the assumption that the entire increase in heat sink temperature corresponds to a decrease in melt energy from its defined "initial" state. This view is flawed since the structures are heated by the thermite burn and radiation from the corium surface in the minutes before water injection and before an "initial melt temperature" is established. Structure preheating is considered in more detail below.

An important source of preheating is thermal radiation from the corium to the inner surfaces of the RV. Water injection begins at t=140 s and so there are about two minutes during which the structures are heated by radiation. The radiative power from the corium surface is given by:

$$Q_{rad} = \sigma \varepsilon A T^4 \tag{5.8}$$

where σ=5.67x10^{-8} W/m^{2}K^4 and A is again the corium surface area (0.071 m^2). The emissivity ε is assumed equal to unity. Radiation from the structures back to the corium has been neglected in the above formulation. For a conservative estimate of Q_{rad}, the corium temperature is set equal to 2000^{o}C (the initial melt temperature is roughly 2300^{o}C). Under these conditions, the instantaneous power radiating from the corium surface is 110 kW and the total energy emitted over 120 s is 13 MJ. A lower emissivity would reduce the heat transfer rate proportionally while slight increases in the melt temperature greatly increase the rate (more than a 50% increase for the initial melt temperature of 2300^{o}C). A more detailed calculation with view factors is not beneficial because, for this analysis, the spatial distribution of the energy deposited in the RV structures is unimportant.

Another source of preheating is convection from hot gases to the inner surfaces of the RV. Figure 5.3 shows the spike in gas temperature at the top of the upper plenum (TG-RV) in the minutes before water injection. At t = 22 s the temperature peaks at 925^{o}C, and then drops to about 230^{o}C just prior to water injection at 140 s. Thus there are about two minutes in which the vessel internals were preheated by convection. Convective heat transfer from the gas to the inner surfaces can be written as:

$$Q_{conv} = h A (T_{gas} - T_{wall}) \tag{5.9}$$

where h is the local heat transfer coefficient over an area A. It is difficult to accurately calculate Q_{conv} because both the heat transfer coefficients and wall temperatures are not well-known. However, the following case is illustrative of the size of the heat transfer: natural convection heat transfer coefficient h~20 W/m^{2}K, total internal area A~1.5m^2, average T_{gas}=500^{o}C, average T_{wall}=200^{o}C; total energy transfer after two minutes is ~1 MJ. A more definitive measure of the total heat transfer would require proper modeling of the heat transfer coefficient, time dependent gas temperature, and inclusion of the thermophysical properties of the structures. Still, the calculation suggests that a non-negligible amount of energy may be transferred to the structures via natural convection, particularly if the heat transfer coefficient is much greater than that selected for the example calculation.

5.4 Implications of corrections

The rate of energy absorption by the heat sinks early in the transient is large and generally exceeds the power deposited in the heat exchanger. The corrections are considerable because the energy required to raise the heat sinks from ambient to saturation temperature (~50 MJ) is a significant fraction of the total energy of the melt (~100 MJ). The proposed corrections include a realistic accounting of the total energy transferred to the heat sinks, but they do not accurately model the rate of energy deposition. There is also uncertainty in the total amount of energy within the system due to the undefined amount of heat transfer to the structures during the period between thermite ignition and water injection.

An unfavorable combination of three factors highlights the need to reduce heat sink effects:

- Total energy transfer to the heat sinks is a substantial fraction of the initial melt energy.
- A large fraction of the melt energy is removed early in the transient.
- Energy transfer to heat sinks is significant for too large a fraction of the total test duration.

Based on this assessment, it is concluded that there is a large uncertainty (~50%) in the heat flux during at least the first half hour of the test (overestimated in the corrected interval and underestimated afterwards). Referring to figure 5.2 one sees that this is nearly ⅓ of the total test duration (after ~6000 s, there is little steam flow to the heat exchanger and the calculated melt energy is very low).

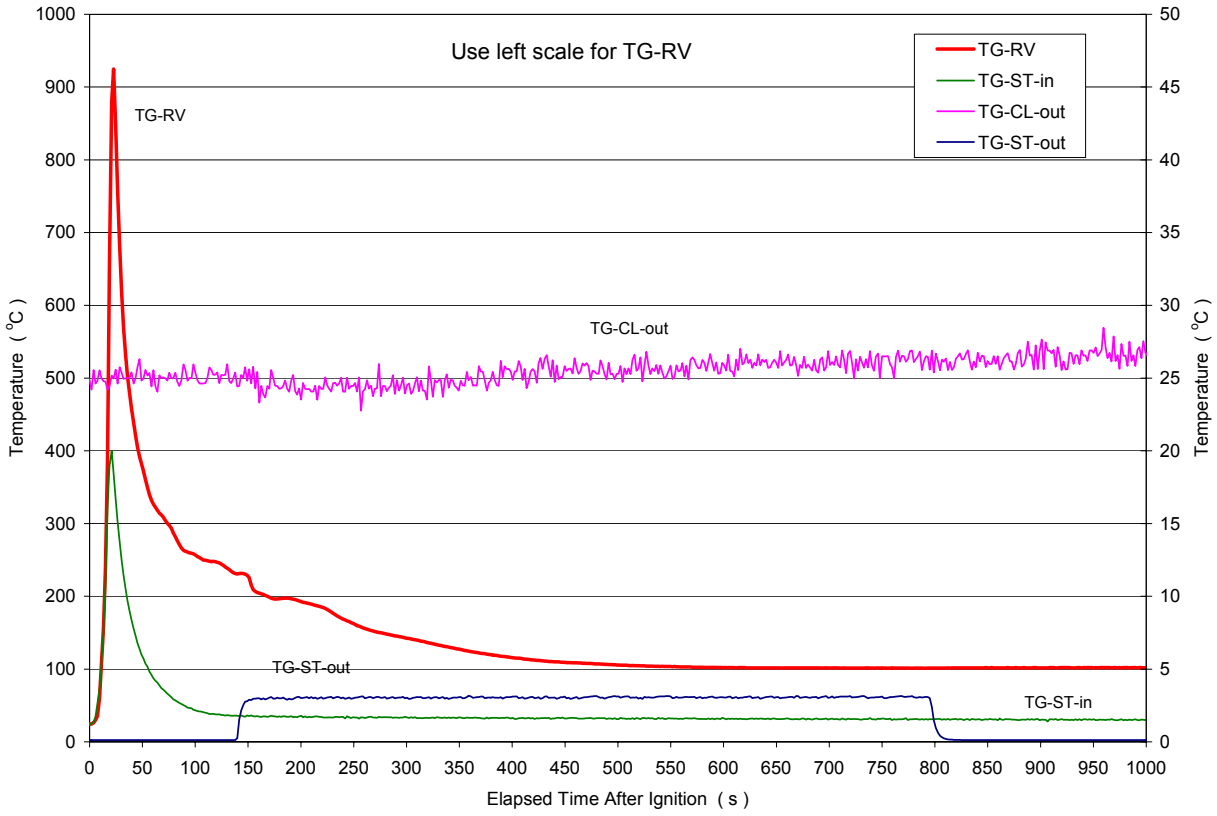

Figure 5.3 Gas temperatures in the RV upper plenum and spray tank.

5.5 Evaluation of dryout heat flux

The melt temperature thermocouple data in figure A.2 provides a second, independent method of evaluating the debris cooling rate to supplement that of the steaming rate. In particular, the dryout heat flux can be evaluated from the following equation that relates the dryout limit to the quench front propagation velocity:

$$q_{dryout} = \rho_c \Delta e \, \mathrm{v} \tag{5.10}$$

where ρ_c = corium density (~6500 kg/m^3), Δe = corium specific enthalpy change upon quench from the initial temperature of ~ 2300 ˚C to water saturation temperature (~1.5 MJ/kg), and v = water ingression rate. The validity of a well-defined quench front is based upon the presumption that cooling is, in the latter stages of the transient, dominated by water ingression and consequently one-dimensional in the axial direction.

As shown in figure A.2, thermocouples located at the melt/base interface indicate arrival of the quench front in the time interval of 6400-7800 seconds. Given the 15 cm melt depth, the quench front propagation velocity is estimated to be in the range of V_{sol} = 6.8-8.3 cm/hour. (recall that cavity flooding was initiated at 140 seconds). Thus, from eq. 5.10, the corium dryout heat flux is estimated to be in the range of 180-225 kW/m^2 based on the rate of propagation of the quench front through the solidifying material. This estimate compares favorably with the plateau in the measured cooling rate, which is about 180 kW/m^2 (figure 5.1).

6. Calculation of the Conduction-Limited Heat Flux

A 3-D model of the RV lower plenum was constructed using the thermal analyzer SINDA/G, which includes both a CAD-type program for preparing the model and a finite-difference code to solve steady-state and transient heat transfer problems. The model is used to estimate the heat flux through the corium surface for the conduction-limited case. Heat losses through the crucible are significant and reduce the heat flux from what would be observed with a perfectly insulating crucible or a large melt pool (the 1-D case). These calculations are therefore essential for providing a conduction-limited heat flux that corresponds to the conditions of the experiment, allowing a meaningful comparison between the measured and conduction-limited heat fluxes.

Figure 6.1 depicts the model created for the lower plenum of the RV. Table 6.1 provides a listing of the dimensions and thermal properties used in the transient calculations. Symmetry has been used to reduce the model to a 1/8th–size slice of the RV. Also, some components were omitted to simplify construction with the CAD interface. These include the mating lower flange (welded around the pipe) and most of the lower plenum wall above the corium.

The initial conditions for the calculations are: a melt temperature of 2300^{o}C and structure temperature (all other components) of 20^{o}C. The melt depth is 15 cm. The heat transfer coefficient from the surface of the corium to the water pool was set to 10 kW/m^{2o}C. This parameter is not critical in these calculations because, soon after the transient begins, heat transfer through the corium surface is limited primarily by the poor conductivity of the corium rather than the heat transfer coefficient at the surface.

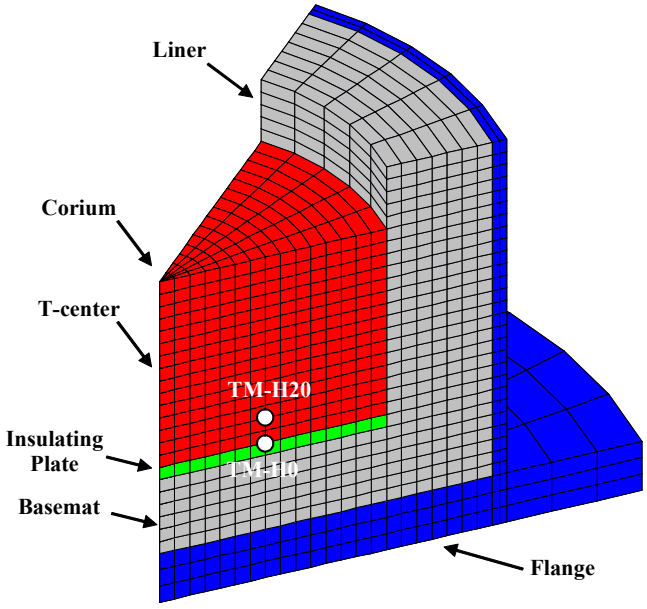

Figure 6.1 Model of reaction vessel lower plenum for SINDA/G.

Table 6.1 Input parameters for SINDA/G model.

Component	Material	Dimensions (cm)	c_p (J/kg°C)	k (W/m°C)	ρ (kg/m^3)
Pipe Wall	Carbon Steel	ϕ45.7x 30 x 0.95	419.	47.	7800.
Lower Flange	Carbon Steel	ϕ63.5 x 4	419.	47.	7800.
Corium	UO_2	ϕ30 x 15	657.	1.5	7000.
Insulating Plate	Cast ZrO_2	ϕ30 x 1	620.	1.2	5500.
Liner	MgO	ϕ43.8 x 24 x 7	1260.	4 to 8	2800.
Basemat	MgO	ϕ43.8 x 6	1260.	4 to 8	2800.

The boundary conditions yet to be defined pertain to the RV outer wall and lower flange. There is, however, some uncertainty in these conditions even though they are vital in determining the radial and axial heat losses through the crucible. The uncertainty arises from inspection of the test data, which shows the lower plenum structure (flange and wall) temperatures rising only to the saturation temperature of 100°C. This contrasts with calculations indicating that the temperature of these structures should rise well above 100°C due to a combination of MgO heating by the corium and a low, natural convection heat transfer coefficient at the outer surface of the structures. The data suggests that steam and/or water passes between the liner and the vessel wall, which holds the wall near the saturation temperature. A small gap between the liner and wall does indeed exist (to permit installation and removal of the liner) and thermocouples placed within the gap for SSWICS2 never measured a temperature above saturation.

The effect of this gap is to cool the outer surface of the crucible with a sink temperature of 100°C via an ill-defined heat transfer coefficient. In addition, one must conclude that the heat flux from

the crucible surface into the gap heats steam and/or water and so it appears as energy deposited in the heat exchanger. This energy must be subtracted from the measured total to obtain the heat transfer rate through the corium surface alone. There is no gap between the basemat and the lower flange and so heat transfer between the two is modeled by conduction. The outer surface of the flange is cooled by natural convection to the ambient air.

The boundary conditions are summarized below:

- Corium surface: convection with h = 10 kW/m^2 ^{o}C to a sink temperature of 100^{o}C (the boiling water pool).
- Lower flange: conduction between basemat and flange, convection with h = 2.5 W/m^2 ^{o}C (calculated from a model for flat vertical plates) to a sink temperature of 20^{o}C.
- The "fin" portion of the upper liner that extends above the corium: convection at the surface with h = 1 kW/m^2 ^{o}C to a sink temperature of 100^{o}C (this area is covered with water and is included in the model to account for the small amount of energy conducted up along the liner and away from the corium).
- Liner outer surface: two cases 1) convection with h = 1 kW/m^2 ^{o}C to a sink temperature of 100^{o}C (it is not known if the surface is in contact predominately with water or steam and so this is a compromise heat transfer coefficient) and 2) the convection heat transfer coefficient reduced to h = 2.5 W/m^2 ^{o}C (to model the extreme case of inefficient cooling of the liner by natural convection in the gap with dry steam).

The results of the calculation are presented in figure 6.1 as heat flux from the corium surface versus elapsed time. The 1-D solution for the same initial conditions and thermophysical properties is included to illustrate the heat flux reduction that accompanies the nonideal system (a crucible that absorbs energy). The data series labeled "Losses 3-D" is the energy transfer rate through the liner and basemat, and it is included for comparison with cooling through the surface alone. All energy transfer rates are scaled by the corium surface area so that they can be compared directly with the data in figure 5.2.

A comparison of the plots in figure 6.1 reveals that heat losses through the sidewalls are a strong function of the boundary condition at the liner surface for the conduction-limited case. This boundary condition, however, has only a modest influence on the calculated corium heat flux itself. Radial losses would be significantly reduced by water ingression because of the higher rate of heat removal through the corium surface. Such an enhanced heat removal rate is indicated by the data, as noted below.

In the bottom plot of figure 6.1 the corrected test data (from figure 5.2) has been combined with the calculated, conduction-limited heat flux so that the two can be compared directly. The plot shows that the measured heat flux was significantly higher than the conduction-limited heat flux through most of the test. Note that late in the test, when the measured heat flux falls below that of the conduction limited solution, there is little thermal energy remaining in the melt.

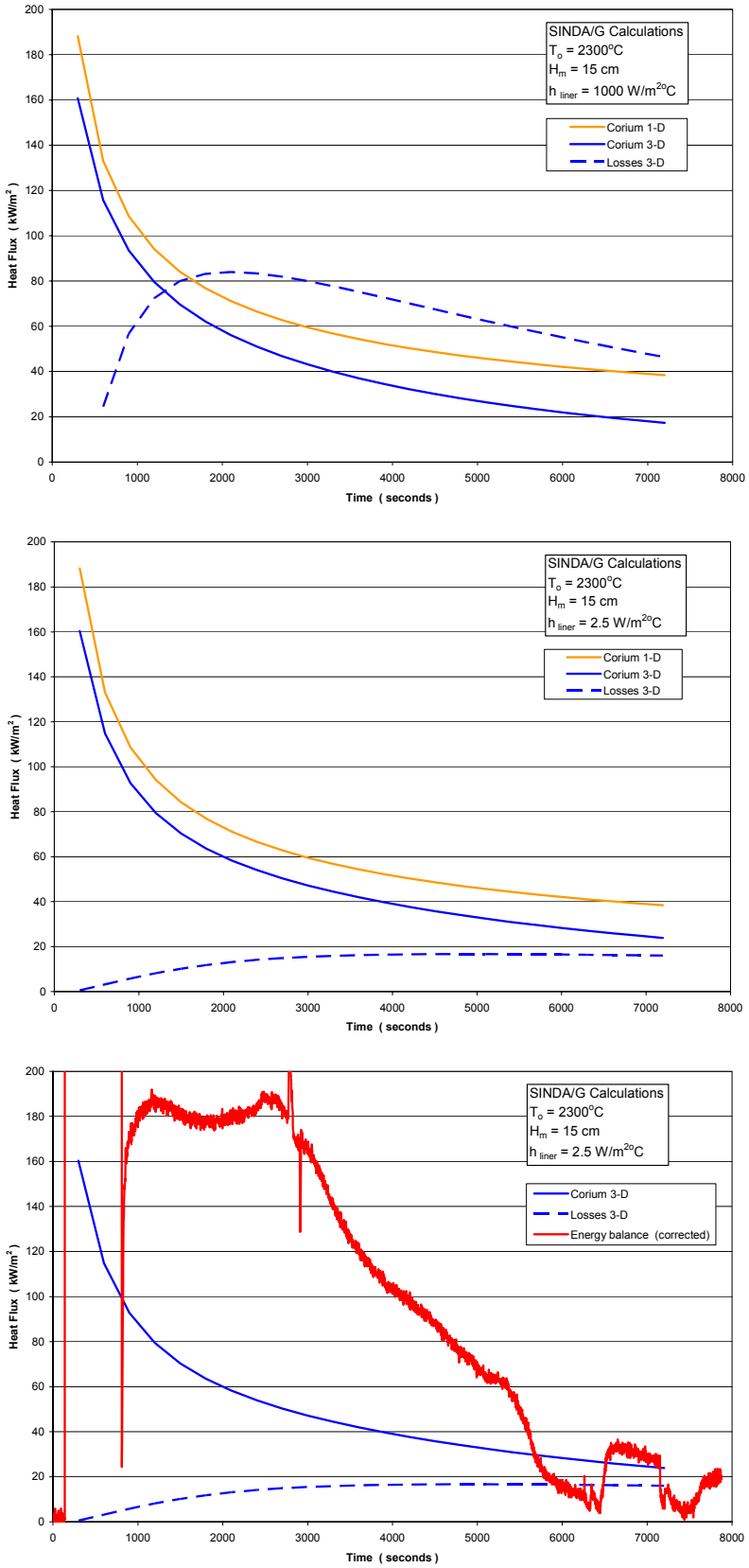

Figure 6.1 Calculated heat flux through corium surface (outer surface of liner cooled by 100°C steam). Top plot: high heat transfer rate akin to boiling; Middle plot: low heat transfer rate, single-phase natural convection. Bottom plot: test data compared with conduction-limited heat flux.

7. Water Percolation Test

The test apparatus was disassembled to separate the various components of the crucible, which is necessary for post-test examinations. The corium had solidified within the lower 12" liner and the two elements were lifted and removed from the basemat as a unit. A top view of the crust is provided in figure 7.1. Above the crust, a layer of frozen corium several millimeters thick is attached to the liner wall (partially removed section visible in the top portion of figure 7.1). The permeability of the crust was measured by pouring water into the liner/crust assembly as described below.

The permeability of a porous material is a parameter that relates the rate of fluid flow through the material to a corresponding pressure drop. The permeability of the corium crust samples is determined by measuring the flow rate of water through the crust with a known driving head. Measurements can be made with either a "constant head permeameter", in which a constant driving pressure maintained, or a "falling head permeameter", in which the driving pressure is allowed to change as water flows through the sample. We have chosen to use a falling head permeameter (fig. 7.1) because it is relatively easy to implement. The following equation, which is derived from Darcy's law, is used to determine the crust permeability κ [1]:

$$\kappa = \frac{L\mu}{\rho g t} \ln(h_0 / h(t)) \qquad (7.1)$$

for a crust thickness L, gravitational acceleration g, liquid density ρ, viscosity μ, water drainage time t, and initial water height h_0.

The falling head permeameter configuration was duplicated by placing the MgO liner with its crust sample into a large container filled with water. The level of the water surrounding the liner was kept even with the top of the crust. The space within the liner above the crust was used for the falling head. Water was poured into the liner until it was full to the top edge, and then it was allowed to flow through the crust and into the surrounding container. The setup is an inverse version of that shown in figure 7.2 with water flowing downwards and the constant level maintained outside and around the sample. The initial head and final heads for each sample were 14 and 2 cm, respectively, and the

Figure 7.1 Solidified corium within MgO liner (top view).

measured drainage times ranged from 64 to 80 s.

The permeability estimate is used to evaluate the dryout limit for comparison with that deduced from the quench rate data. For example, the following expression for the limiting heat flux in a porous medium can also be derived from Darcy's law:

$$q''_d = \frac{0.5 h_{lv} \kappa \rho_l g}{\nu_v} \qquad (7.2)$$

given the latent heat of vaporization h_{lv}, liquid density ρ_l , and steam kinematic viscosity ν_v. The dryout heat fluxes calculated from the permeability data are plotted in figure 7.3

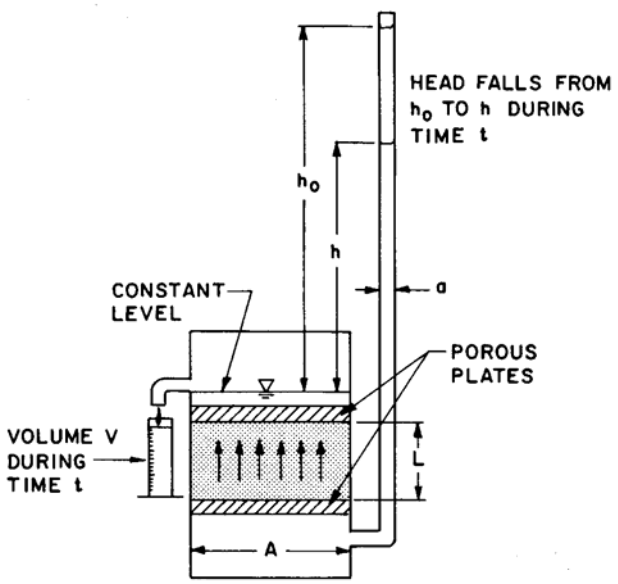

Figure 7.2 Falling head permeameter (Bear, 1972).

For accurate measurements of permeability, and therefore dryout heat flux, the permeameter must be constructed so that fluid is unable to bypass the sample. A good seal between the crust and the MgO liner is required to avoid an erroneously high value of κ. Subsequent examinations of the crust, in which air was forced up through the bottom while a water layer was on the top, indicated that the joint between the liner and the crust is permeable. During these tests, one could observe bubbles rising from both the crust surface and the seam with the liner. It is not possible to quantify the effect of this leakage on κ, but it is clear that leakage increases the

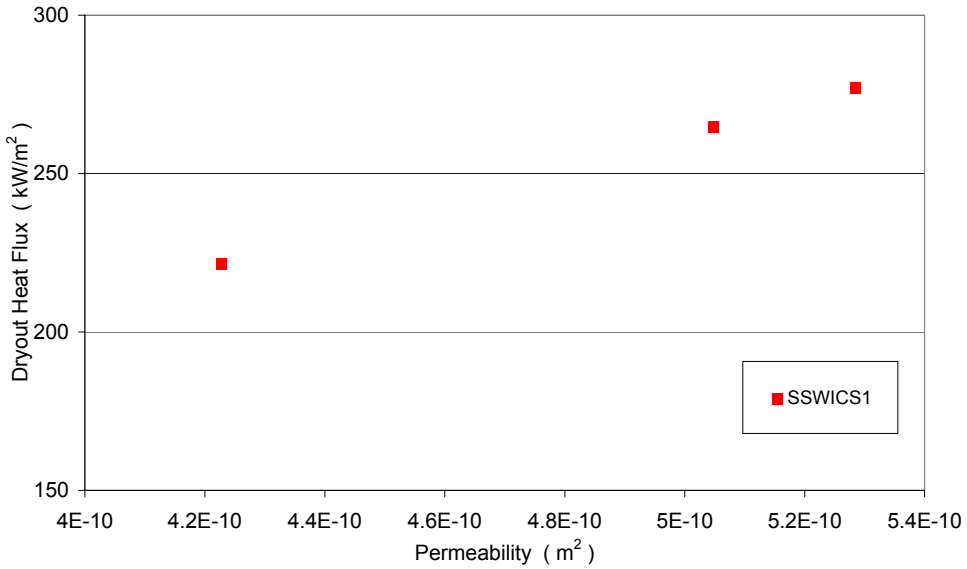

Figure 7.3 Dryout heat flux data derived from permeability measurements

apparent permeability and thus the calculated dryout heat flux. It would therefore be difficult to regard the dryout heat fluxes plotted in figure 7.3 as conservative. The permeability measurements could be improved by removing the crust from the liner and mounting it in a special apparatus that permits the construction of an effective seal.

8. Crust Strength Test

The mechanical strength of the crust will be tested using a specially constructed device that loads the crust with a hydraulic press (figure 8.1). The size of the load is measured while it is slowly increased until the crust fails. Test results were not available at the time of this report. They shall appear in future revisions.

References

[1] J. Bear, Dynamics of Fluids in Porous Media, American Elsevier Co., 1972.

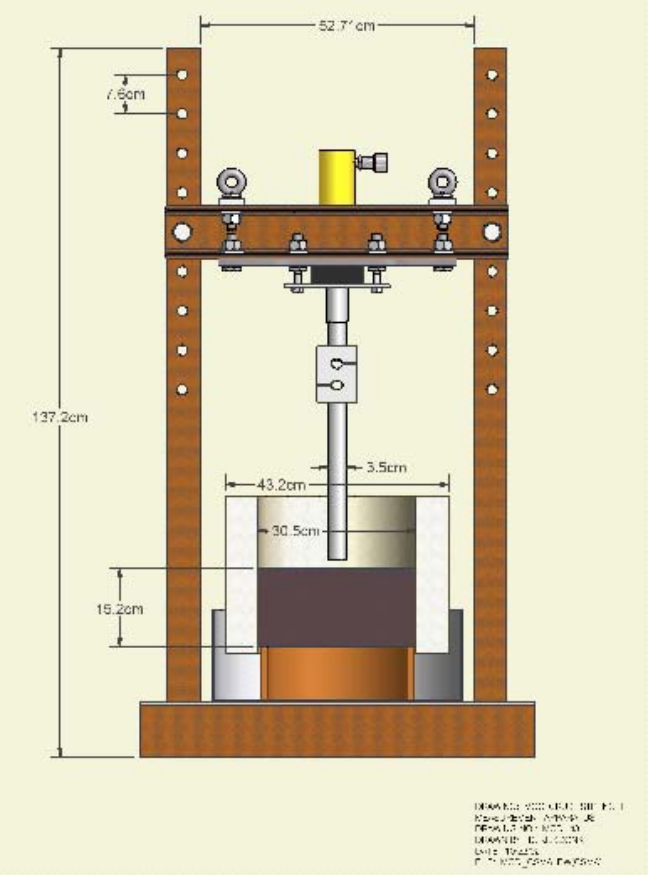

Figure 8.1 Crust strength apparatus

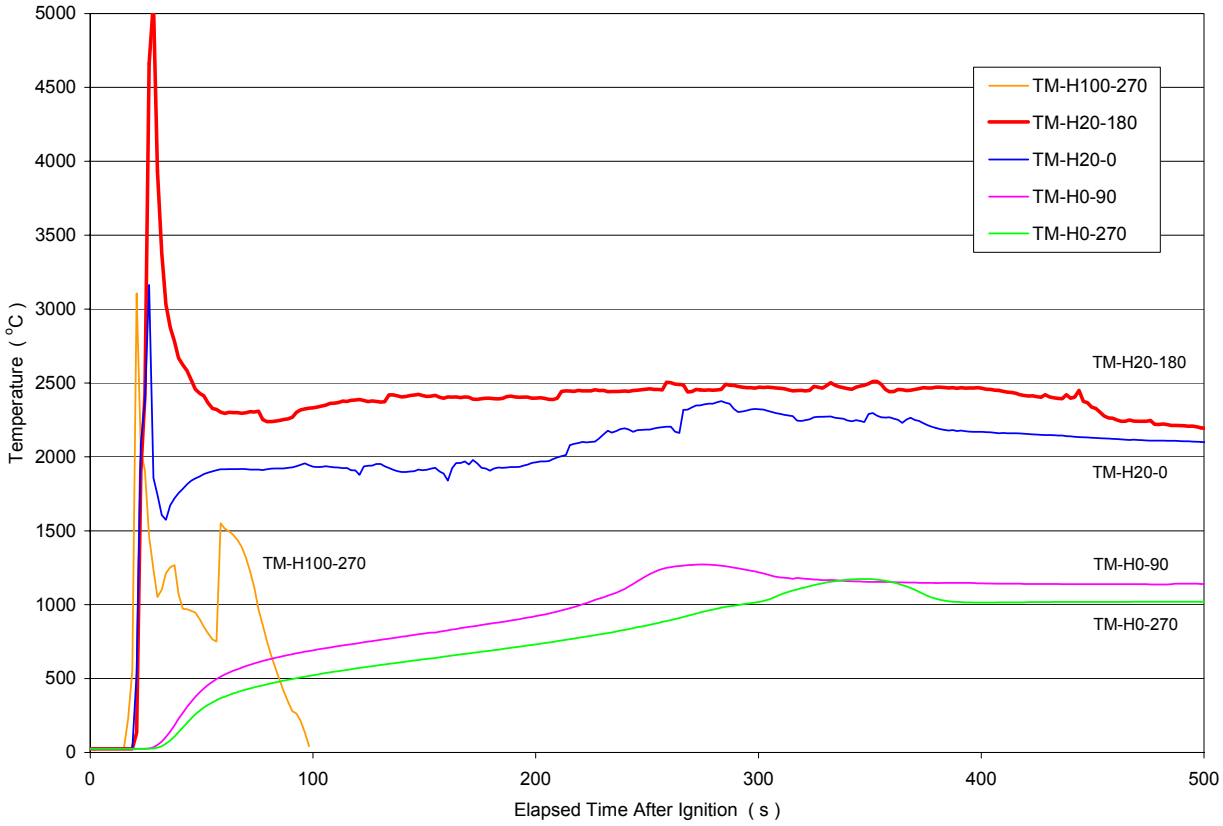

Figure A.1 Melt temperatures early in the transient.

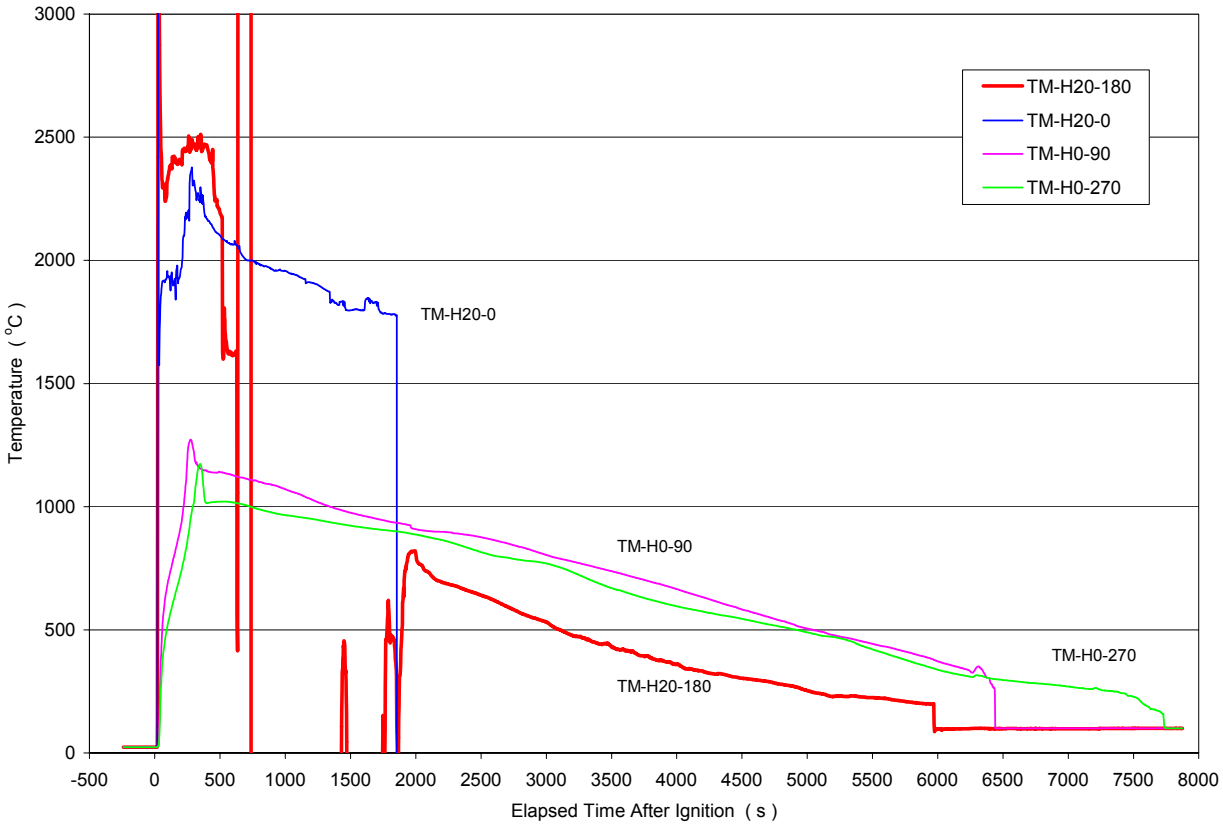

Figure A.2 Melt temperatures for the entire test duration.

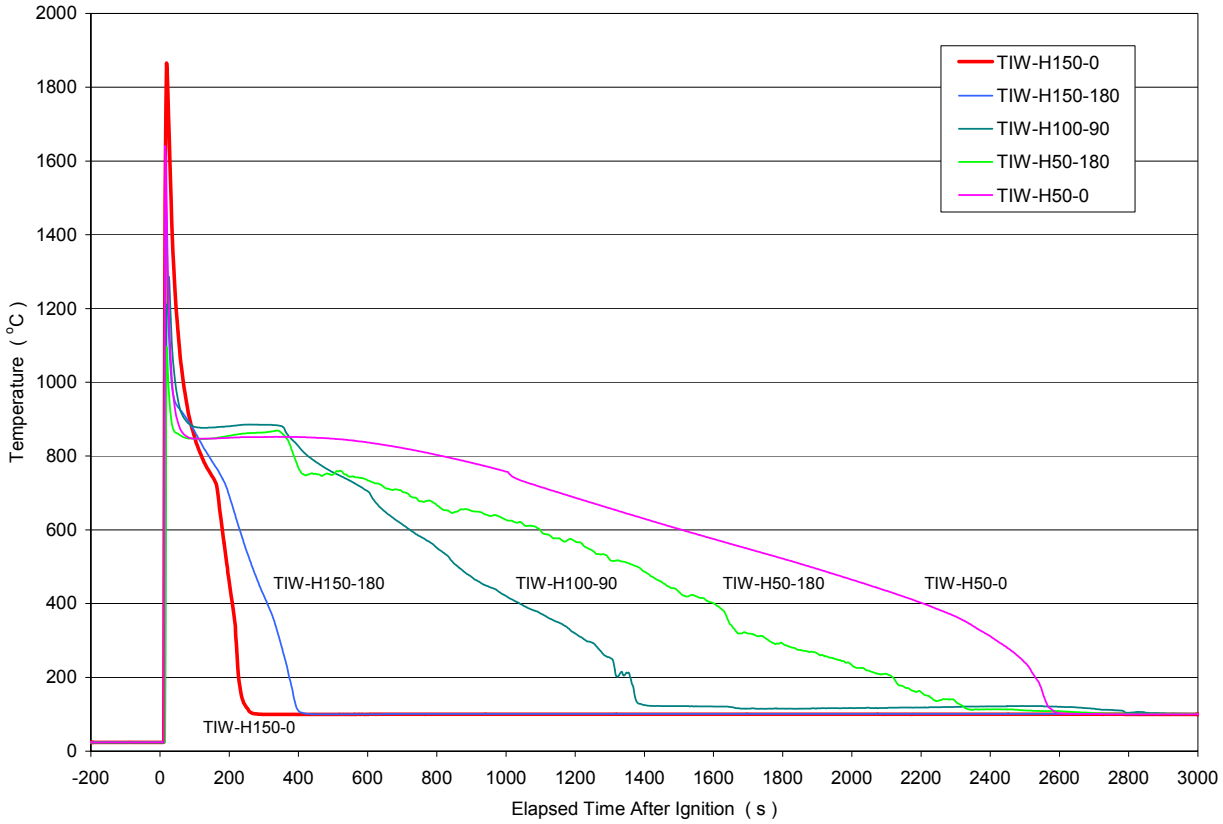

Figure A.3 Temperatures at the inner wall of MgO insulator.

Figure A.4 Structure temperatures.

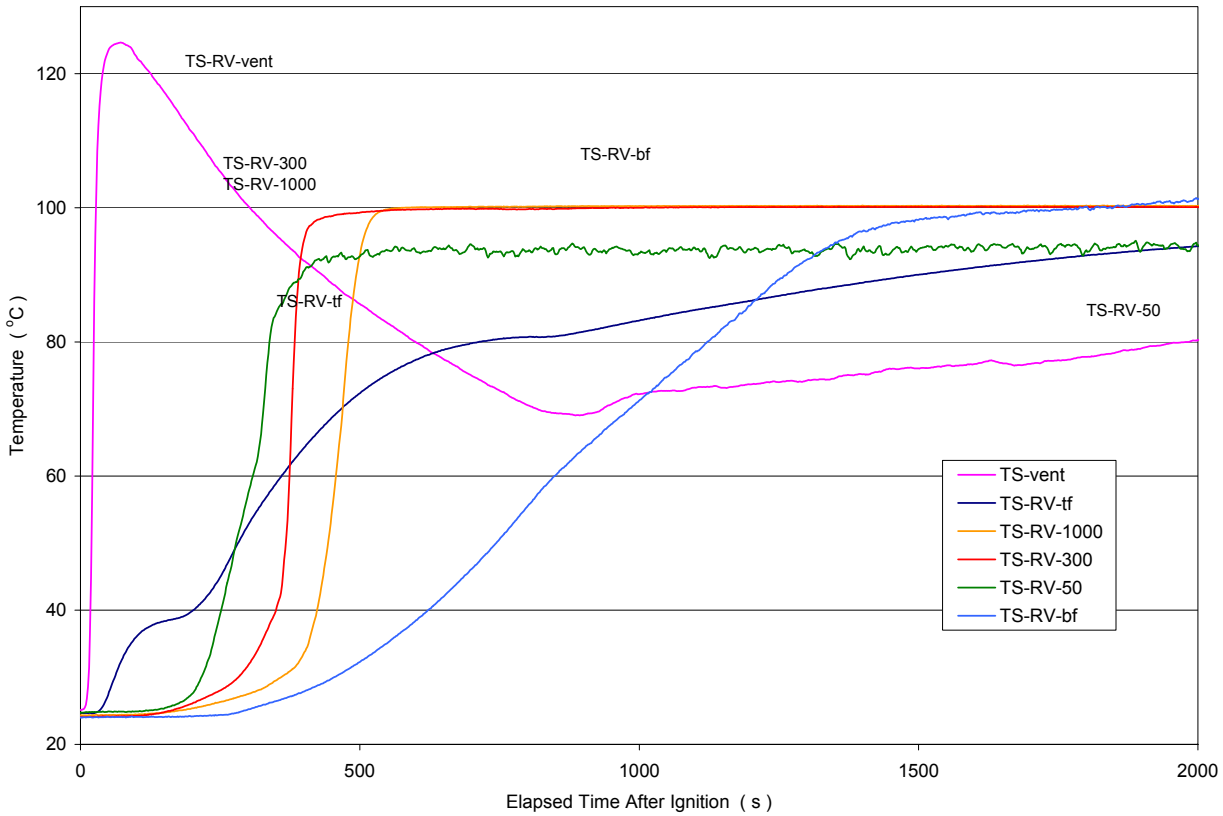

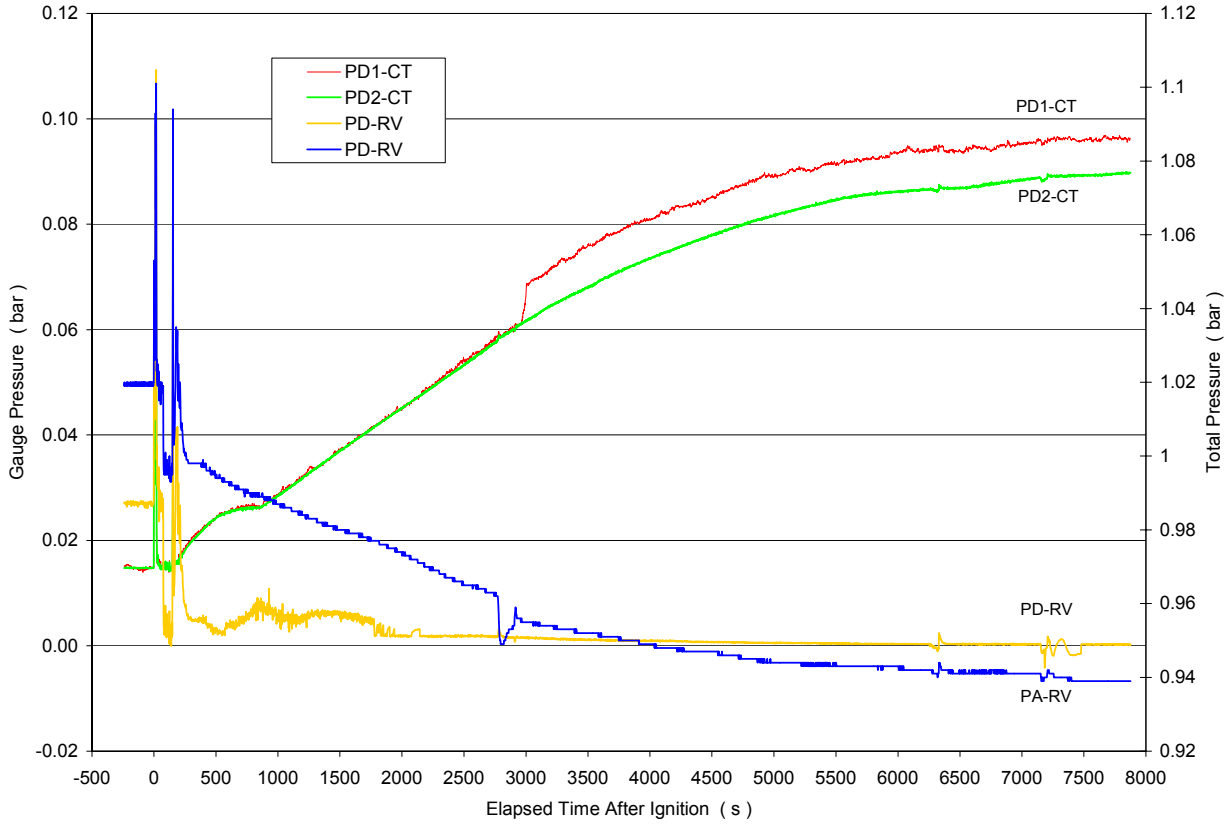

Figure A.5 Pressure and ΔP in RV and condensate tank.

Figure A.6 Water injection into RV and HX secondary side flow rate.

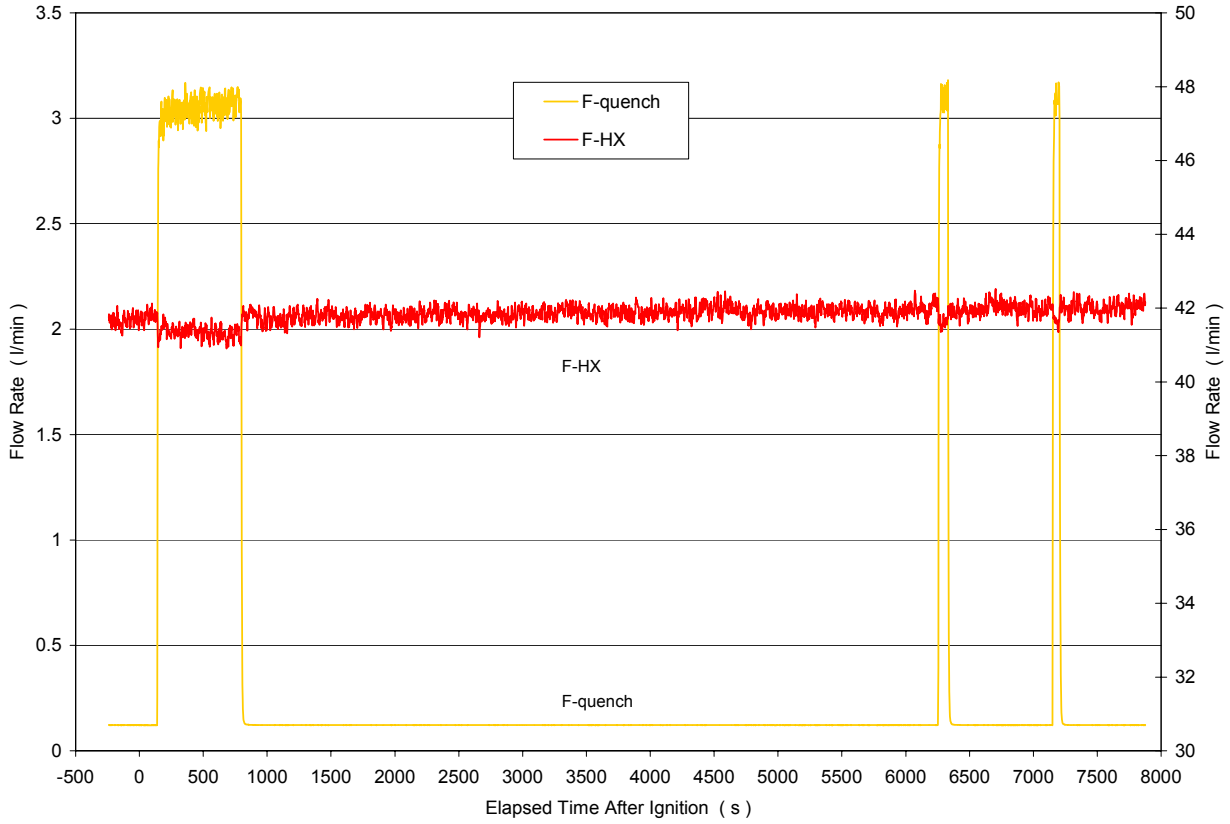

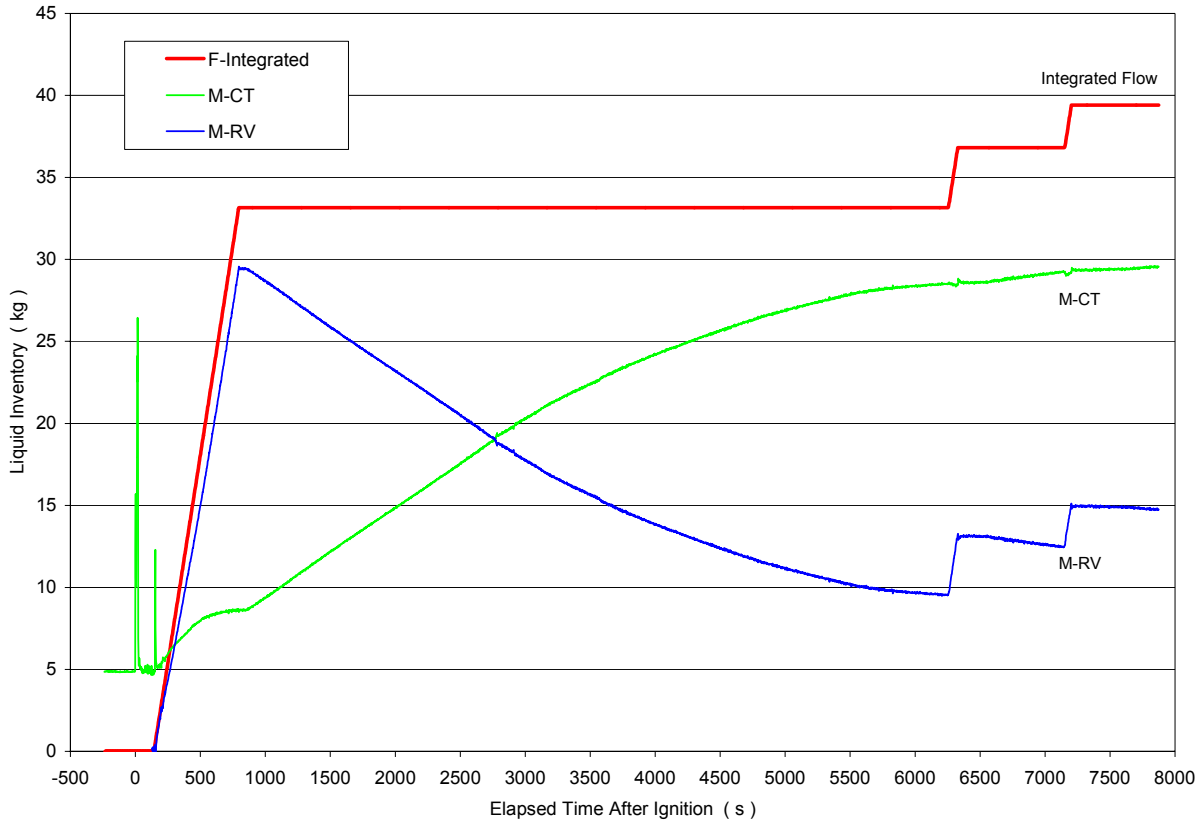

Figure A.7 Integrated quench flow and calculated RV liquid inventory.

Figure A.8 Secondary side fluid temperatures at HX inlet and outlet.

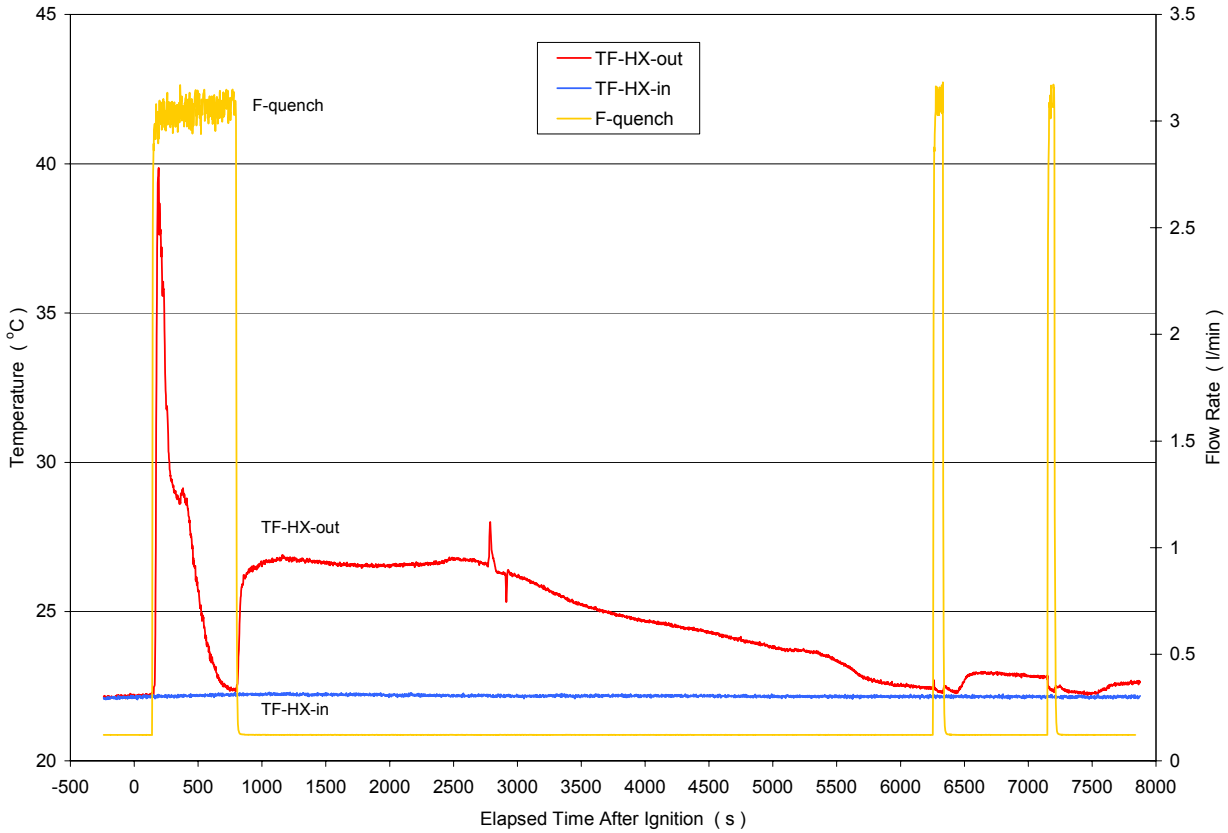

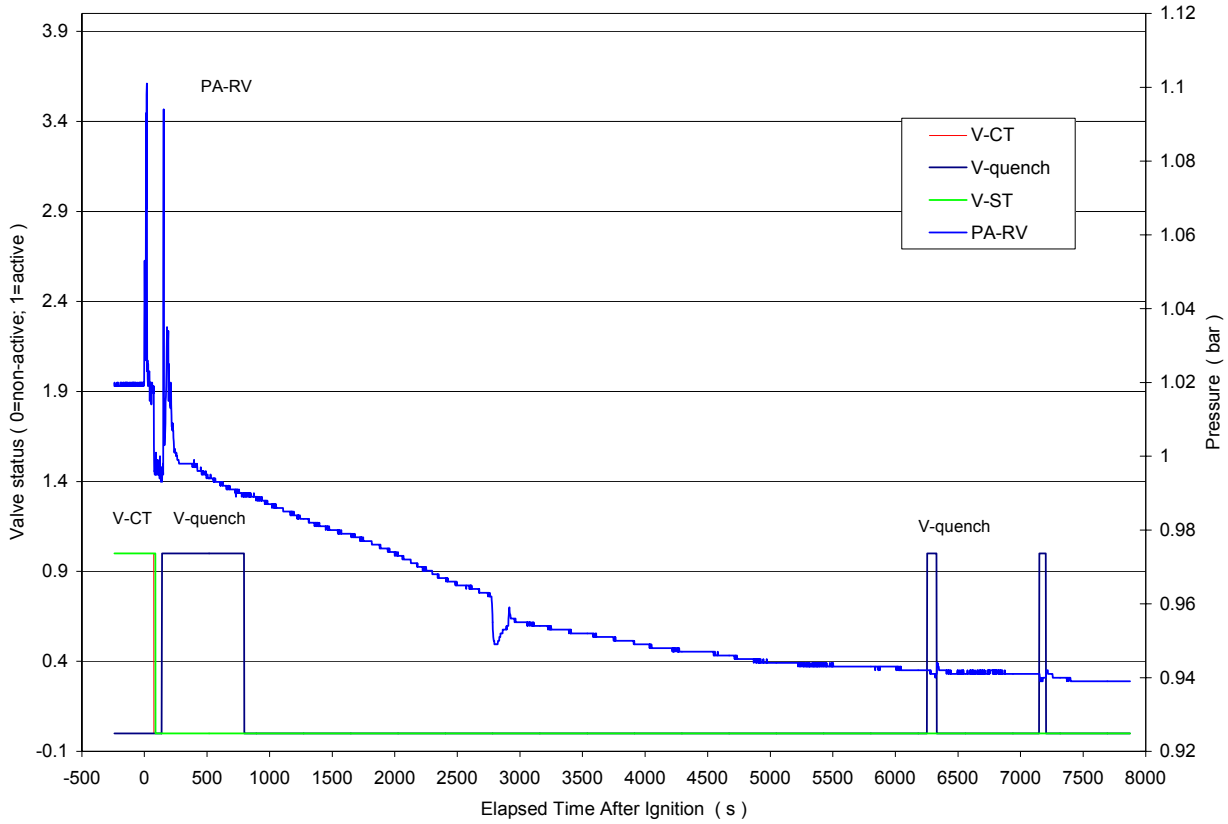

Figure A.9 Valve status during course of test.
Figure A.10 Measured heat flux at RV (insulated) and vent line (uninsulated) surfaces.

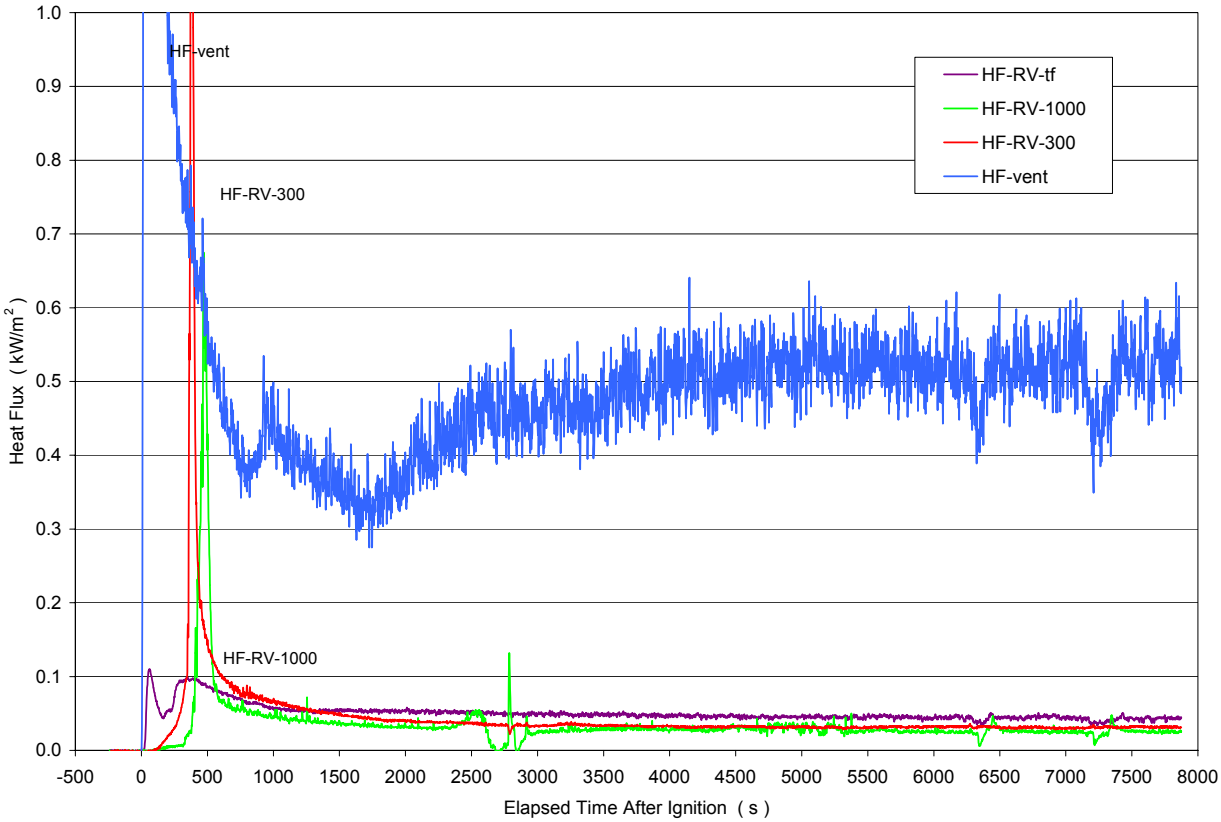

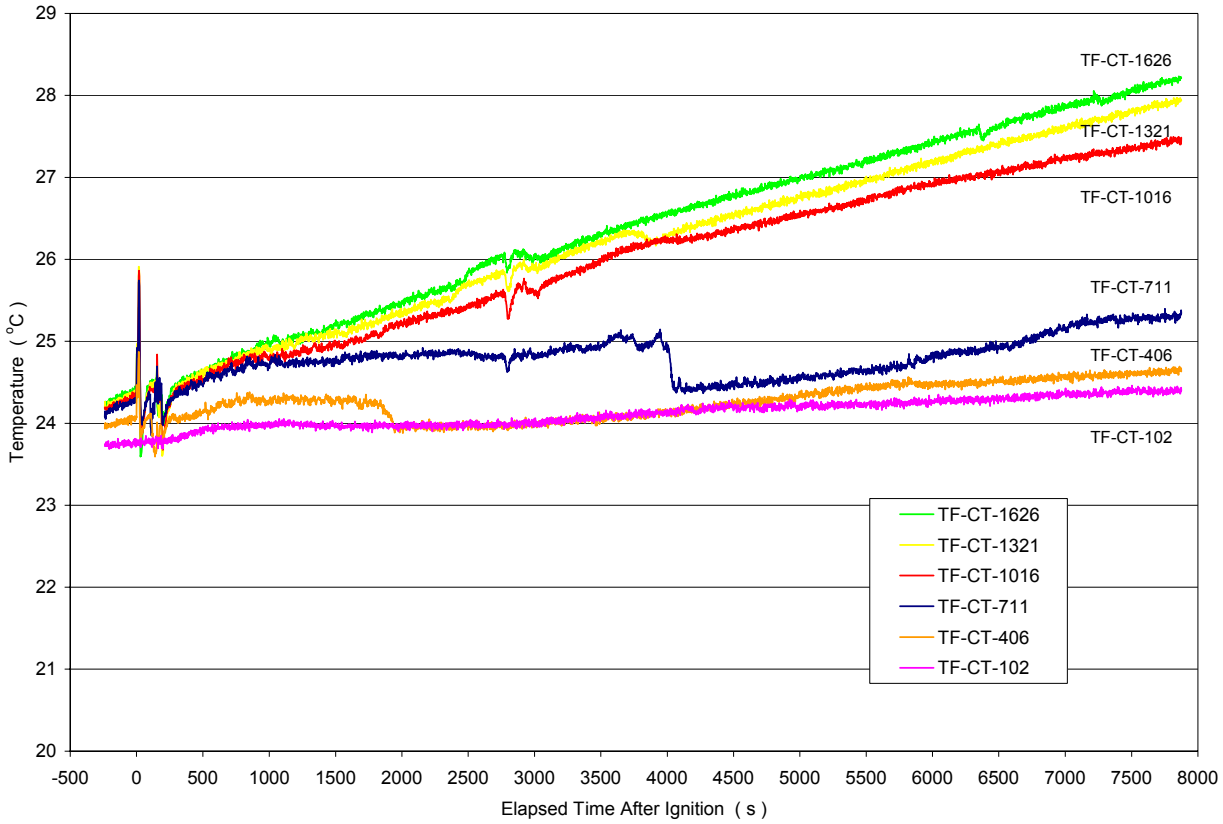

Figure A.11 Fluid temperatures in the condensate tank.

Figure A.12 Heat flux through corium (uncorrected).